Glass-like Thermal Conductivity Induced by Oxygen Vacancies in Nanoscale Epitaxial $La_{0.5}Sr_{0.5}CoO_{3-\delta}$

X.W. Wu,[a] J. Walter,[b] T.L. Feng,[c] J. Zhu,[a] H. Zheng,[d] J.F. Mitchell,[d] N. Biškup,[e] M. Varela,[e] X.L. Ruan,[c] C. Leighton,[b] X.J. Wang,[a]

[a]Department of Mechanical Engineering
University of Minnesota, Twin Cities, 111 Church Street S.E., Minneapolis, MN 55455, USA

[b]Department of Chemical Engineering and Material Science
University of Minnesota, Twin Cities, 421 Washington Ave. S.E., Minneapolis, MN 55455, USA

[c]School of Mechanical Engineering and the Birck Nanotechnology Center
Purdue University, West Lafayette, IN 47907, USA

[d]Materials Science Division, Argonne National Laboratory, Argonne, IL 60439, USA

[e]Departamento de Fisica de Materiales & Instituto Pluridisciplinar
Universidad Complutense de Madrid, Madrid, 28040 Spain
(Previous address: Materials Science & Technology Division, ORNL. Oak Ridge, TN 37831, USA)

MARCH 2017

SUBMITTED TO

ACS NANO

Glass-like Thermal Conductivity Induced by Oxygen Vacancies in Nanoscale Epitaxial $La_{0.5}Sr_{0.5}CoO_{3-\delta}$

X.W. Wu,[a] J. Walter,[b] T.L. Feng,[c] J. Zhu,[a] H. Zheng,[d] J.F. Mitchell,[d] N. Biškup,[e] M. Varela,[e] X.L. Ruan,[c] C. Leighton,[b] X.J. Wang,[*,a]

[a]Department of Mechanical Engineering, University of Minnesota, Twin Cities, 111 Church Street S.E., Minneapolis, MN 55455, USA

[b]Department of Chemical Engineering and Material Science, University of Minnesota, Twin Cities, 421 Washington Ave. S.E., Minneapolis, MN 55455, USA

[c]School of Mechanical Engineering and the Birck Nanotechnology Center, Purdue University, West Lafayette, IN 47907, USA

[d]Materials Science Division, Argonne National Laboratory, Argonne, IL 60439, USA

[e]Departamento de Fisica de Materiales & Instituto Pluridisciplinar, Universidad Complutense de Madrid, Madrid, 28040 Spain (Previous address: Materials Science & Technology division, Oak Ridge National Laboratory. Oak Ridge, TN 37831, USA)

ABSTRACT

We report the application of time-domain thermoreflectance (TDTR) to extract the through-plane thermal conductivity of $La_{1-x}Sr_xCoO_{3-\delta}$ (x = 0.5, LSCO) epitaxial thin films of varying thickness (3 to 18 nm) on $LaAlO_3$ (LAO) and $SrTiO_3$ (STO) substrates. These LSCO films possess spatially ordered oxygen vacancies with $\delta \approx 0.1$ that are the primary means of lattice mismatch accommodation with the substrate; compressive/tensile strain thus controls the orientation of the oxygen vacancy order (OVO). TDTR results reveal that the room temperature thermal conductivities of LSCO on both substrates (~1.7 W m^{-1} K^{-1}) are nearly a factor of four lower than that of bulk single crystal LSCO (6.2 W m^{-1} K^{-1}). Remarkably, this approaches the lower limit of amorphous oxides (*e.g.*, 1.3 W m^{-1} K^{-1} for amorphous glass), with no dependence on the OVO orientation. Boltzmann transport equation (BTE) and molecular dynamics (MD) simulations were performed to better interpret these results. Both BTE and MD elucidate that oxygen vacancies have a more pronounced effect than Sr substitution in suppressing thermal conductivity. According to the cumulative thermal conductivities of LSCO from a BTE model, the close-to-amorphous-limit (or glass-like) thermal conductivity is in part due to truncation of phonon modes with mean free paths longer than the film thickness. The absence of dependence on the OVO orientation is also validated by MD, and is rationalized in terms of two competing effects: anisotropic thermal transport from the OVO, and the reduction of thermal conductivity due to the enhanced phonon scattering.

KEYWORDS: *thermal conductivity, TDTR, LSCO, oxygen vacancy, molecular dynamics simulation, Boltzmann transport equation*

1. INTRODUCTION

The remarkable functionality of perovskite oxides, encompassing superconductivity,[1] piezoelectricity,[2] ferroelectricity,[3] thermoelectricity,[4-5] mixed ionic conductivity,[6] and ferromagnetism,[7] suggest their potential use in a wide range of applications, in solid oxide fuel cells,[8] as superconductors,[1,9-10] in resistive memory devices,[11] and in thermoelectric devices.[5,12-14] These are in addition to existing use in ferroelectric memories, tunable capacitors, etc.[3,15-17] Largely responsible for this great range of functionality is the ability of the perovskite structure (with ABO_3 as its general formula) to incorporate a large fraction of the metals in the periodic table on either the A or B cationic site. This flexibility allows for the tuning of many functionalities by substitution of A and/or B site cations, as well as by control of oxygen stoichiometry (i.e., by inducing oxygen vacancies or interstitials). One such example is in strontium-doped lanthanum cobaltite, $La_{1-x}Sr_xCoO_{3-\delta}$ (LSCO), in which divalent Sr^{2+} substitution for La^{3+} hole-dopes the initially insulating and non-ferromagnetic $LaCoO_3$ (LCO), increases the formal Co valence, and induces metallic ferromagnetism via a spin-state transition.[18-19]

Control of the oxygen stoichiometry has been shown similarly effective in tuning the properties of LSCO. Oxygen vacancies compensate Sr-induced holes, destabilizing metallicity and ferromagnetism, and thus controlling both. Moreover, the presence of oxygen vacancies has been shown to critically influence the high oxygen conductivity that makes LSCO an excellent candidate for gas separation membranes,[20] gas sensors,[21] and solid oxide fuel cell cathodes.[8,22] Oxygen vacancies readily form above $x = 0.5$ in LSCO due to the general instability of Co^{4+} in octahedral coordination.[23] This is also evidenced by the very high oxygen pressure needed to form $SrCoO_3$ ($x = 1$),[24] and the tendency of $SrCoO_{3-\delta}$ to form $Sr_2Co_2O_5$ ($SrCoO_{2.5}$), the so-called Brownmillerite structure, with *ordered* oxygen vacancies.[25-27] The Brownmillerite structure is derived from perovskite when oxygen vacancies form in alternating (001) Co-O planes, along staggered [110] lines, resulting in alternating planes of tetrahedrally- and octahedrally-coordinated Co ions. In thin film form, $SrCoO_{3-\delta}$ can be made to undergo reversible redox reactions between Brownmillerite and epitaxial phases, with intriguing potential applications.[28-30]

Notably, while Bulk LSCO at x = 0.5, unlike x = 1, does not readily form in the Brownmillerite structure, *epitaxial films* of LSCO at x = 0.5 do exhibit oxygen vacancy ordering.[31-36] In essence, a brownmillerite-like structure is induced in these films, and is understood to be the primary accommodation mechanism for the lattice mismatch between LSCO and single crystal perovskite substrates. In the case of a compressive mismatch, for instance, such as the 1.2% mismatch produced by $LaAlO_3$(001) (LAO) substrates, the oxygen-vacancy-ordered (OVO) planes run parallel to the film/substrate interface, enabling out-of-plane expansion, and in-plane compression, to match the substrate.[31] With a tensile mismatch, such as the −1.8% mismatch produced by $SrTiO_3$ (001) (STO) substrates, the OVO planes run perpendicular to the film/substrate interface, enabling in-plane expansion to match the substrate.[31] This is a unique mechanism of lattice mismatch accommodation, not relying on misfit dislocations. Engineering of this oxygen vacancy ordering with the choice of substrate, and thus the lattice mismatch generated, has been shown to tailor several properties of LSCO epitaxial films, including strain relaxation[31] and low temperature redox activity[28].

As a fundamental transport property, thermal conductivity can provide a wealth of information on the scattering processes for charge and thermal carriers in materials. For perovskite oxides specifically, studies of thermal transport properties are of particular interest to advance potential applications such as thermal barriers[37] and thermoelectric materials,[14,38-40] due to their structural versatility, and their thermal and chemical stabilities at high temperatures.[38,41]

While there have been numerous studies of the electrical, magnetic, structural and mechanical properties of LSCO thin films,[31-33,36,42-52] the thermal transport properties of LSCO thin films have yet to be studied. The majority of published studies have rather focused on the thermal properties of *bulk* LSCO crystals or polycrystals with different concentrations of Sr.[53-55] Special attention has been given to the thermally- or doping-induced spin-state transition, and on suppression of thermal transport in polycrystalline LSCO with varying defects and grain sizes, for potential thermoelectric applications.[56-58] As for thermal transport in perovskite oxide films other than LSCO, a few studies[4,38,59-62] have been carried out on the suppression of thermal conductivities of STO films with point defects,[60] planar defects,[38,60] and oxygen vacancies.[62] These studies have identified thermal transport measurements as a useful approach to probing general structural perfection/defects in STO films.

In light of the above, epitaxial LSCO films present an intriguing model system for studying the general structure-property relations between oxygen vacancies (including their ordering) and thermal transport in oxide films. However, LSCO film thicknesses typically have to be quite low (*e.g.*, less than 20 nm) in order to preserve the structural control of oxygen vacancy ordering, and to prevent strain relaxation.[31,33] This restriction to the very low thickness regime due to the need to avoid strain relaxation is not unique to LSCO films, but is general to epitaxial oxides, where coherent strain is often utilized as a powerful method to tune properties. Such ultrathin films thus pose a grand challenge in thermal science, where characterization of thermal transport properties is non-trivial.

To address this fundamental, yet technologically important, structure-property correlation, we utilize here time-domain thermoreflectance (TDTR)[63-66] to reveal how the “built-in” oxygen vacancies in epitaxial LSCO films, serving as controllable point defects at the atomic level, impact the thermal transport in these films. Such studies on LSCO films can not only lend insight into the general effects of oxygen vacancies on thermal transport in oxide films, but also on whether the *ordering* of oxygen vacancies can induce anisotropy in thermal transport, when compared with electrical transport. The effective through-plane thermal conductivities of a series of epitaxial LSCO films of varying thickness (from 6 to 18 nm) are obtained here from TDTR, from which the through-plane thermal conductivities of LSCO epitaxial films are extracted. Comparisons are made between films with OVO planes perpendicular and parallel to the through-plane thermal transport direction, using films grown on LAO and STO, respectively. Computational modeling including both Boltzmann transport equation (BTE) and molecular dynamics (MD) methods are applied to explain the fundamental mechanisms of phonon transport in the LSCO epitaxial films, elucidating a number of unanticipated observations. In particular, we obtain glass-like thermal conductivity values which approach the amorphous limit, despite the single crystallinity of the LSCO films, with remarkably weak thermal anisotropy. These features are mainly ascribed to the combined effects of point defects of oxygen vacancies and Sr substitution, the size effect resulting from the ultralow film thickness, and weak electron/phonon coupling within the LSCO film.

2. EXPERIMENTAL METHODS

2.1. Sample Synthesis and Structural Characterization

We grew LSCO (x = 0.5) thin films on commercial substrates using high-pressure oxygen sputtering from homemade $La_{0.5}Sr_{0.5}CoO_3$ polycrystalline targets, as previously reported.[67] Substrates were first annealed at 900 °C in 1 Torr of flowing O_2, followed immediately by film growth at 600 ^{o}C. This was achieved with 66 W of DC sputter power in 1.4 Torr of O_2, with post-deposition cooling in 600 Torr of O_2. Films grown by this method have been subject to thorough prior structural and chemical characterization using high-resolution wide-angle X-ray diffraction (WAXRD), rocking curve analysis, grazing incidence in-plane diffraction, grazing incidence X-ray reflectivity, cross-sectional scanning transmission electron microscopy (STEM), electron energy loss spectroscopy (EELS), and scanning probe microscopy.[31-33,48,51] Two types of epitaxial thin-film samples were studied: LSCO films grown on (001)-oriented LAO substrates (type A) and LSCO epitaxial films grown on (001)-oriented STO substrates (type B). Both sample types A and B consist of a series of LSCO films with varying thicknesses (3, 6, 8.5, 12.5, and 18 nm). The representative WAXRD data presented here were obtained using a Panalytical X'Pert Pro system using monochromatic Cu $K_{\alpha,1}$ (λ = 1.5406 Å) radiation. The atomic resolution STEM images were acquired in a Nion Ultrastem 100 equipped with a spherical aberration corrector and a Gatan Enfinium spectrometer at the Oak Ridge National Laboratory. TEM specimens were prepared by conventional methods, including grinding and ion milling. For comparison, *bulk* single crystals of LSCO (nominally x = 0.3) (sample type C) and LCO, were also prepared for thermal characterization, using floating zone methods.[68] The choice to use an x = 0.3 crystal for comparison, as opposed to an x = 0.5 crystal, was enforced by the difficulty of growing x = 0.5 single crystals without high oxygen pressures. x = 0.3 and x = 0.5 are expected to be essentially identical from structural and electronic perspectives, and in both cases the oxygen vacancy density is known to be low, from numerous physical property measurements.[68] The single-crystal, single-phase nature of the LSCO and LCO bulk crystals was confirmed by X-ray and neutron diffraction measurements.[68-70] Bare LAO and STO commercial substrates were also measured as a reference.

2.2. Ultrafast Thermal Measurements

Time-domain thermoreflectance, an ultrafast-laser based technique,[71-74] was applied to extract the thermal conductivities of LSCO epitaxial films, bulk single crystals of LSCO, and substrates of LAO and STO.[72,75-76] Each sample was coated with an Aluminum (Al) layer of ≈70 nm, serving as a metal transducer. The thermal conductivity of the Al transducer was calibrated *via* four-point probe measurements coupled with Wiedemann-Franz Law estimates, prior to TDTR.[77-78] For each sample we conducted TDTR measurements at 2 modulation frequencies (1.6 and 9 MHz) and obtained its thermal conductivity by simultaneously fitting two sets of dual-frequency TDTR data to a thermal diffusion model.[66] The ultrafast TDTR experimental setup and more details about the system are presented in Fig. S1 and in Section S1 of the Supporting Information.

3. THEORETICAL MODELING

3.1. Thermal Diffusion Modeling for Layered Structures

The essential structural components of our LSCO samples, from top to bottom, include Al, the Al/LSCO interface, the LSCO epitaxial film, the LSCO/substrate interface, and the substrate (LAO or STO), as shown in Fig. 1.

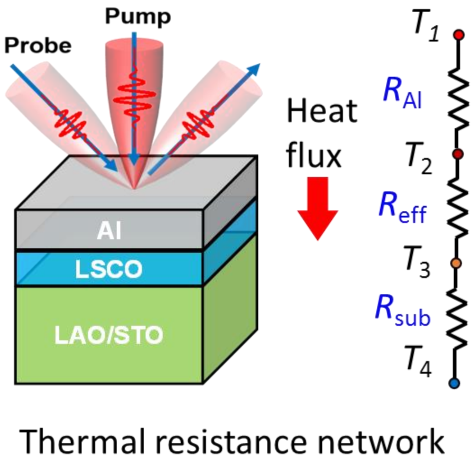

Figure 1. Schematic of the TDTR measurement on the sample stack consisting of an Al transducer, LSCO epitaxial film, and the substrate. The heat flux is imposed at the Al transducer layer and passes through a thermal resistance network in series with the multilayer structure.

Due to the ultrathin film nature of the LSCO epitaxial films (3 to 18 nm), thermal waves penetrate through the entire LSCO film and are sensitive to both interfaces, and the LSCO film sandwiched in between. This leads to a challenge in the direct fitting of TDTR data to simultaneously extract the thermal conductivity of the LSCO film (Λ_{LSCO}), as well as the interfacial thermal resistances at the Al/LSCO interface (R_{I1}) and LSCO/substrate interface (R_{I2}). To resolve this, we define an effective thermal resistance R_{eff} as[79-80]

$$R_{\mathrm{eff}} = \frac{h_{\mathrm{LSCO}}}{\Lambda_{\mathrm{eff}}} = R_{\mathrm{I1}} + \frac{h_{\mathrm{LSCO}}}{\Lambda_{\mathrm{LSCO}}} + R_{\mathrm{I2}} \tag{1}$$

where Λ_{eff} is the effective thermal conductivity combining the contributions from the LSCO film (Λ_{LSCO}) and two interfaces (R_{I1} and R_{I2}), and h_{LSCO} is the LSCO thickness (varying from 3 to 18 nm). Values of Λ_{eff} can be directly extracted from TDTR data for LSCO samples of different thicknesses. To a first approximation, R_{I1} and R_{I2} are presumed independent of LSCO thickness for these series of epitaxial films on the same substrate, as justified by, among other factors, the identical deposition conditions. With this approximation, R_{eff} becomes linearly proportional to

h_{LSCO} with a slope of $1/\Lambda_{\text{LSCO}}$, and the sum of R_{I1} and R_{I2} is the intercept at zero film thickness. Strictly speaking, Λ_{LSCO} would also be expected to change with h_{LSCO}, considering the enhanced boundary scattering of phonons with mean free paths (MFPs) longer than the thicknesses of LSCO epitaxial films. Therefore, Λ_{LSCO} from Eq. (1) is treated here as an apparent value, averaged over single-crystal LSCO epitaxial films on the same substrate with varying thicknesses (3 to 18 nm). The assumption of largely thickness-independent Λ_{LSCO} by neglecting phonon dispersion is also justified by the BTE predicted cumulative thermal conductivity (Λ_{cumu}) of LSCO as a function of phonon MFP, as detailed below in Section 4.3. Also, it should be noted here that our discussion is based on the assumption that Λ_{LSCO} is dominated by the lattice contribution, due to the weak electron-phonon coupling both at the interfaces and inside the correlated LSCO films (Section 4.4). This should render small the impact of any finite size or dead layer effects[32-33,67] in the electronic contribution to Λ_{LSCO}.

3.2. Boltzmann Transport Equation

To better interpret the measurement results, and understand the suppression of thermal transport in LSCO, we apply the BTE to calculate the lattice thermal conductivity using:[81]

$$\Lambda_{1} = \frac{4\pi}{3}\frac{1}{(2\pi)^3}\sum_{\nu}\int \frac{\hbar^2\omega^2(\mathbf{k},\nu)}{k_{\mathrm{B}}T^2}\frac{e^{\frac{\hbar\omega(\mathrm{k},\nu)}{k_{\mathrm{B}}T}}}{\left(e^{\frac{\hbar\omega(\mathrm{k},\nu)}{k_{\mathrm{B}}T}}-1\right)^2} v^2(\mathbf{k},\nu)\tau(\mathbf{k},\nu)k^2 dk \qquad (2),$$

summing the contributions of all the phonon branches with the index ν. In Eq. (2), $\omega(\mathbf{k},\nu)$, $v(\mathbf{k},\nu)$, and $\tau(\mathbf{k},\nu)$ are the angular frequency, group velocity, and relaxation time of the phonon mode $(\mathbf{k},\nu)$, respectively, with $\mathbf{k}$ representing the phonon wave vector. The phonon frequency and group velocity are calculated with lattice dynamics (LD) by using a hybrid interatomic potential described by the core-shell model, the short-range Buckingham potential, and long-range Coulombic forces.[82] This hybrid potential has been demonstrated to reproduce well the lattice structure, mechanistic features, vacancy energy, doping energy, oxygen ion migration energy, and surface polarization of bulk $LaCoO_3$ crystals.[82-84]

The phonon relaxation time τ, the inverse of the scattering rate for the phonon mode $(\mathbf{k}, \nu)$, is calculated by the Matthiessen rule,[81,85]

$$\frac{1}{\tau(\mathbf{k},\nu)} = \frac{1}{\tau_{\mathrm{p}}(\mathbf{k},\nu)} + \frac{1}{\tau_{\mathrm{Sr}}(\mathbf{k},\nu)} + \frac{1}{\tau_{\mathrm{O_V}}(\mathbf{k},\nu)} + \frac{1}{\tau_{\mathrm{b}}(\mathbf{k},\nu)} \quad (3).$$

The terms on the right side of Eq. (3) are the scattering rates induced by lattice anharmonicity (τ_{p}), La/Sr alloy mass disorder (τ_{Sr}), oxygen vacancies (τ_{Ov}), and sample boundaries due to finite dimensions (τ_{b}, neglected for bulk), respectively. More details on the hybrid potential and BTE calculation such as corresponding phonon dispersions (Fig. S2), normalized phonon density of state (DOS) (Fig. S3), and phonon relaxation time spectra (Fig. S4) are provided in Section S2 of the Supporting Information.

3.3. Molecular Dynamics Simulations

Molecular Dynamics simulations were performed to reveal the OVO effect on the lattice thermal conductivities of LSCO epitaxial films. The values of lattice thermal conductivity were calculated by the Green-Kubo method based on equilibrium molecular dynamics performed using LAMMPS, according to the formula[86]

$$\Lambda_{\mathrm{l},\mathbf{z}} = \frac{1}{k_{\mathrm{B}} T^2 V} \int_0^{\infty} \langle S_{\mathbf{z}}(t) S_{\mathbf{z}}(0) \rangle \, dt \quad (4)$$

where **z** denotes the transport direction, V is the simulation domain volume, and $S_{\mathbf{z}}$ represents the heat current in the **z** direction. The angular brackets indicate the heat current auto-correlation functions (HCACF).[86] (Results for HCACF of LSCO samples are shown in Fig. S5 in Section S3 of the Supporting Information) The potential functions employed in MD simulations are those used in the LD calculations, but without the core-shell model, since the core-shell model is not applicable in MD simulations due to the zero mass of the shell. Such simplification does not affect the lattice structure or the low-energy phonon dispersion, as demonstrated by the good agreement between calculated phonon dispersion and measurement data from inelastic neutron scattering (see details in Fig. S6 in Section S3 of the Supporting Information), and thus will not affect the thermal conductivity calculations much. The Coulomb interaction cutoff radius in the MD simulations was set as 11 Å, and the interactions outside the cutoff are computed in reciprocal space via an Ewald summation.

4. RESULTS AND DISCUSSION

4.1. Structural Characteristics of LSCO Epitaxial Thin Films

Figures 2a and 2b show WAXRD scans of the (002) substrate and LSCO film peaks for Type A and B samples, respectively, at a representative thickness of 18 nm. Qualitatively, both scans show well-defined (002) film peaks and Kiessig fringes; the LSCO films are epitaxial with low roughness, with compressive and tensile lattice mismatches as expected for Type A and B samples, respectively. The substrate and LSCO film out-of-plane lattice parameters (calculated based on the (002) film peak position) are summarized in Table 1. Reciprocal space maps (not shown) demonstrate these films to be pseudomorphic with the substrate, exhibiting no strain relaxation for film thicknesses < 20 nm. As previously reported, the nominal compressive (1.2%

for LAO) or tensile (−1.8% for STO) lattice mismatch at the LSCO/substrate interface is accommodated by the formation of long-range OVO planes that are either horizontally (on LAO) or vertically (on STO) aligned within the LSCO epitaxial films.[31] These OVO planes are shown in the high resolution *Z*-contrast STEM images in Figs. 2c and 2d as alternating bright (oxygen sufficient) and dark (oxygen deficient) Co-O planes. Figures 2e and 2f are illustrative schematics of the OVO structure observed for Type A and B samples, respectively, based on the Brownmillerite structure. The schematics show the resulting shift of Co ions (black spheres) into tetrahedral coordination upon formation of oxygen vacancies (white spheres) in alternating planes and along [110] lines for Type A samples and [-101] lines for Type B samples, as well as the resulting shift of La/Sr ions (green spheres) toward the O stoichiometric planes. Transparent blue polyhedra are used to differentiate the O-deficient layers (tetrahedral, lighter) from the O-stoichiometric layers (octahedral, darker).

Note that to emphasize and illustrate the OVO structure, the stoichiometry in Figs. 2e and 2f was set to exactly $La_{0.5}Sr_{0.5}CoO_{2.5}$ (*i.e.* $\delta = 0.5$), which is the brownmillerite structure. This is not, however, the exact structure that forms in these LSCO films, which have δ considerably less than 0.5. Estimates based on previously reported EELS data (see Supporting Information Fig. S7) indicate $\delta \approx 0.09$ on LAO, and $\delta \approx 0.11$ on STO. We take this as $\delta \approx 0.1$ in later modeling. Note that these estimates are subject to significant absolute systematic uncertainties of ~0.05, but their relative uncertainties are much smaller (~0.01). The main point is that some of the oxygen vacancy sites in the schematics shown here are actually occupied in the films. We thus know that OVO is present in these films, the direction in which it forms, but not the precise distribution of oxygen vacancies.[31-32] Details of the sample structural characteristics are summarized in Table I.

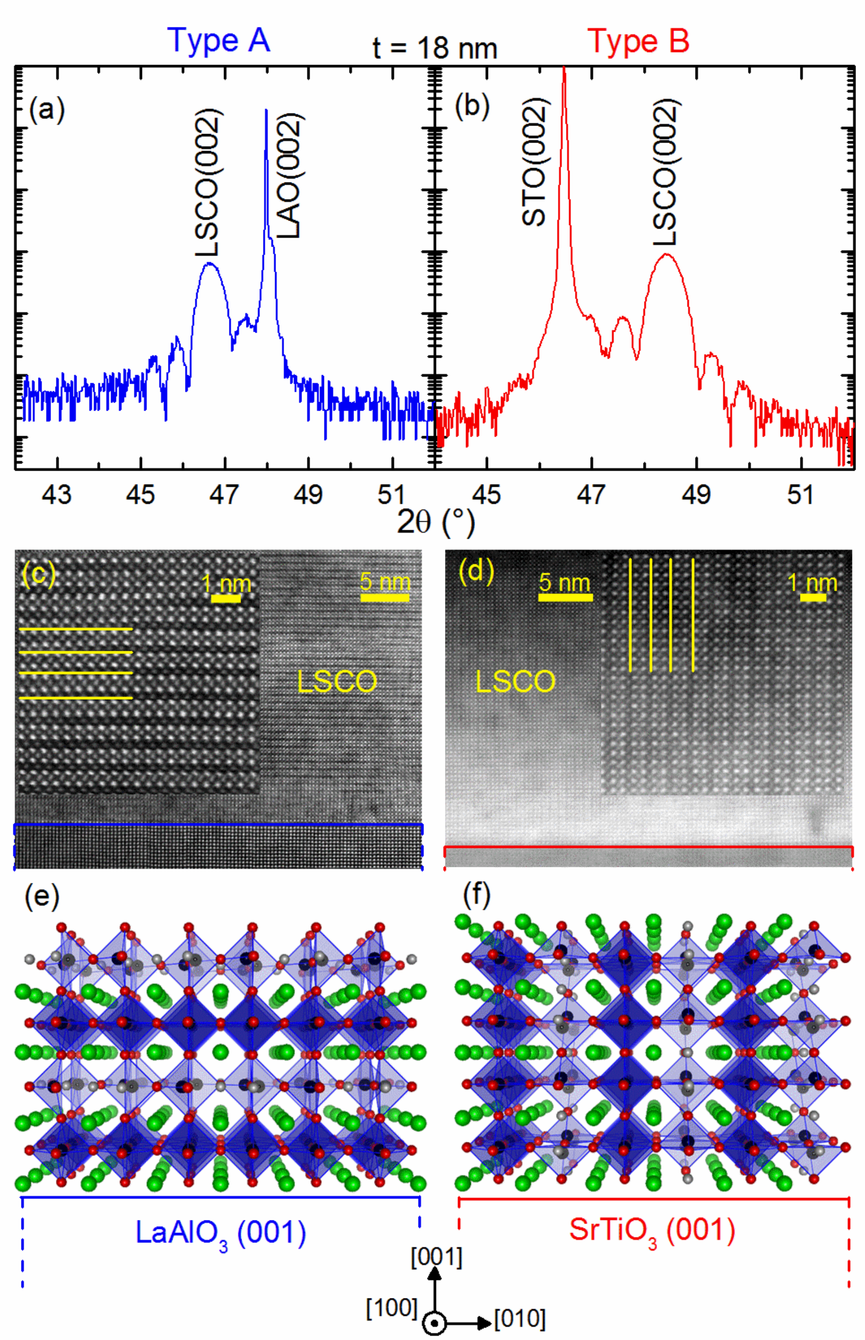

Figure 2. (a) and (b) are specular WAXRD scans for 18-nm-thick films on LAO (Type A) and STO (Type B), respectively. (c) and (d) are high resolution *Z*-contrast STEM images of the substrate-film interface regions in Type A and B samples, respectively. Blue and red lines mark the substrate-film interface and yellow lines mark O-deficient planes. (e) and (f) are crystal structure schematics along the [100] zone axis for Type A and B samples, respectively. Coordinate axes are labeled beneath the diagrams. The color scheme for the ions is as follows: Co (black), La/Sr (green), O (red), oxygen vacancy (white). Transparent blue polyhedra (both tetrahedral and octahedral) are used to emphasize the difference between O-stoichiometric (octahedral, darker) and O-deficient (tetrahedral, lighter) planes.

Table I. Structural parameters of the $La_{1-x}Sr_xCoO_{3-\delta}$ samples and substrates. Note that films in this 3-18 nm thickness (h_{LSCO}) range are pseudomorphic with both substrates, exhibiting no strain relaxation, as determined using reciprocal space maps (not shown).

Sample	h_{LSCO}	x	δ	a	b	c	OVO	Structure
	(nm)			(Å)	(Å)	(Å)		
A. LSCO/LAO	3-18	0.5	~0.09	3.789	3.789	3.890	Horizontal	Tetragonal
B. LSCO/STO	3-18	0.5	~0.11	3.905	3.905	3.760	Vertical	Tetragonal
C. LSCO	Bulk	0.3	~0	5.393	...	13.20		Rhombohedral (α_R=60.5°)
LAO (sub)	Bulk	…	…	5.365	...	13.11		Rhombohedral (α_R=60.1°)
STO (sub)	Bulk	…	…	3.905	...	…		Cubic
LCO	Bulk	0	~0	5.342	...	13.01		Rhombohedral (α_R=61.1°)

4.2. TDTR Experimental Results

Figure 3 illustrates the representative TDTR signals and associated best fitting to extract Λ_{eff} for LSCO epitaxial films (samples A and B in Table I) on LAO and STO substrates. The thickness of the Al transducer determined from the picosecond acoustics of the in-phase signal is 70 nm (Fig. 3a).[76,87] In typical TDTR measurements, the in-phase signal (V_{in}) represents the time evolution of the temperature excursion of the Al transducer. The out-of-phase signal (V_{out}) is approximately proportional to the imaginary part of the temperature oscillations at the modulation frequency. The ratio of V_{in} and V_{out} signals ($-V_{\mathrm{in}}/V_{\mathrm{out}}$) from TDTR experimental data at dual modulation frequencies of 1.6 and 9 MHz for the 3- and 18-nm LSCO epitaxial films are shown in Figs. 3b and 3c. The fitting of the ratio signals with the thermal diffusion model for a multi-layer structure allows the extraction of Λ_{eff} , and thus the thickness-dependent R_{eff}.[66]

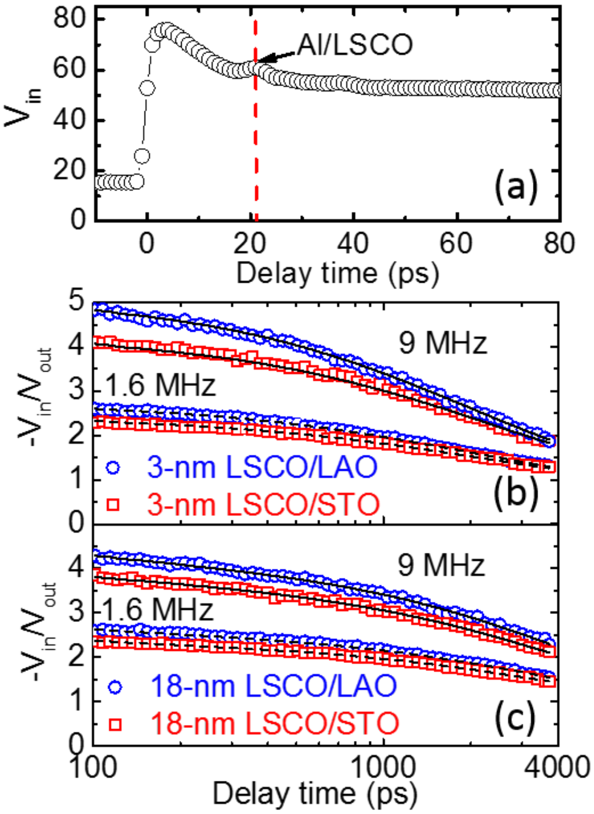

Figure 3. (a) Picosecond acoustic signals from the LSCO epitaxial film sample for determining the thickness of the Al transducer. (b) and (c) are TDTR ratio signals and fitting results for the 3-nm LSCO and 18-nm LSCO films on LAO (blue circles) and STO (red squares) substrates, respectively. All the samples are measured at dual modulation frequencies of 1.6 and 9 MHz. Solid lines (9 MHz) and dashed lines (1.6 MHz) represent the best-fit representations of measurements using the thermal diffusion modeling.

Here, R_{eff} is the lumped thermal resistance shown in Eq. (1), which consists of contributions from interfacial thermal resistances at the Al/LSCO and LSCO/substrate interfaces and the thermal resistance of the LSCO epitaxial films (Fig. 1). The values of R_{eff} are plotted as a function of LSCO film thickness in Figs. 4a and 4b. The uncertainties on R_{eff} from TDTR measurements are evaluated based on a sensitivity analysis; they range from 11% to 15% for all LSCO films of different thicknesses on both substrates (see details in Section S4 of the Supporting Information). To obtain the thermal conductivity of LSCO epitaxial films, we applied

Eq. (1) to linearly extrapolate R_{eff} to zero film thickness. Note here that we excluded the 3 nm data in this linear fitting, since the sum of interfacial thermal resistances ($R_{\mathrm{I1}} + R_{\mathrm{I2}}$) for films of $\leqslant$ 3 nm will decrease dramatically due to a coherent phonon effect associated with the extremely low film thickness.[88] In this case ($h_{\mathrm{LSCO}} \leqslant 3$ nm), the assumption of thickness-independent $R_{\mathrm{I1}} + R_{\mathrm{I2}}$ fails, and R_{eff} deviates from linearity as a function of h_{LSCO}. This phenomenon has also been experimentally observed before.[79] As illustrated in Figs. 4a and 4b, the excellent linear dependence of R_{eff} on h_{LSCO}, excluding the 3 nm LSCO data, validates the approximation of thickness-independent thermal interfacial resistance for films thicker than 3 nm. The fitting process results in $\Lambda_{\mathrm{LSCO}} = 1.69 \pm 0.25$ W m^{-1} K^{-1} for LSCO on LAO substrates and $\Lambda_{\mathrm{LSCO}} = 1.73 \pm 0.22$ W m^{-1} K^{-1} (for uncertainty analysis see Section S4 of the Supporting Information) for LSCO on STO substrates. Surprisingly, this suggests no apparent dependence of Λ_{LSCO} on oxygen vacancy ordering direction.

For completeness, we further attempted to fit R_{eff} for LSCO films of all thicknesses and found that the inclusion of the 3 nm LSCO does not significantly influence the dependence of Λ_{LSCO} on oxygen vacancy ordering. Rather, it only decreases Λ_{LSCO} from ~1.7 to ~1.5 W m^{-1} K^{-1} for LSCO epitaxial films on both LAO and STO substrates. Although the ordering of oxygen vacancy planes does not have observable effects on Λ_{LSCO}, remarkably, the value of $\Lambda_{\mathrm{LSCO}} = 1.7$ W m^{-1} K^{-1} approaches the amorphous limit (~1.3 – 1.4 W m^{-1} K^{-1}). To our knowledge, this is the first time that this has been reported for single-crystal oxide materials.

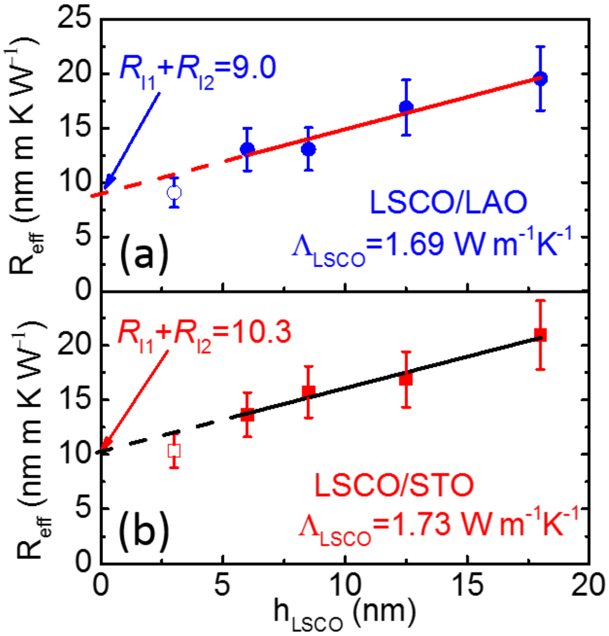

Figure 4. Linear fitting of R_{eff} of LSCO epitaxial films with varying thicknesses on LAO (a) and STO (b) substrates. The thermal conductivity of LSCO from fitting is $\Lambda_{\mathrm{LSCO}} = 1.69$ W m^{-1} K^{-1} for sample A and $\Lambda_{\mathrm{LSCO}} = 1.73$ W m^{-1} K^{-1} for sample B, respectively. R_{eff} is the lumped thermal resistance consisting of contributions from interfacial thermal resistances at Al/LSCO and LSCO/substrate interfaces (intercept of the linear fit in Figs. 4a and 4b) and from the thermal resistance of the LSCO epitaxial films (slope of the linear fit in Figs. 4a and 4b).

The intercept from linear fitting of R_{eff} to $h_{\mathrm{LSCO}} = 0$ is the combined interfacial thermal resistance, $R_{\mathrm{I1}} + R_{\mathrm{I2}}$, of the Al/LSCO interface and LSCO/substrate interface. $R_{\mathrm{I1}} + R_{\mathrm{I2}}$ is found to be 9.0×10^{-9} m^2 K W^{-1} for LSCO films on LAO substrates (sample A) and 10.3×10^{-9} m^2 K W^{-1} for LSCO films on STO substrates (sample B). Though a ~10% difference of $R_{\mathrm{I1}} + R_{\mathrm{I2}}$ is found between sample A and sample B, this is still within the measurement uncertainty.

To understand the factors that cause the large suppression of the thermal conductivity in these samples, we also measured the thermal conductivities of bulk single crystals of LSCO ($x = 0.3$), LCO, and the two substrates, LAO and STO (Table II). The thermal conductivity

(6.2 W m^{-2} K^{-1}) of the bulk $La_{0.7}Sr_{0.3}CoO_3$ crystal (sample C in Table I) is 40% less than that of the LAO (~13 W m^{-1} K^{-1}) and STO (~11 W m^{-1} K^{-1}) bulk crystals. We attribute this reduction of thermal conductivity to Sr substitutions for La, which act as point defects, scattering heat-carrying phonons. The thermal conductivity of LCO bulk single crystals was found to be ~2.2 W m^{-1} K^{-1}, which is ~80% smaller than that of LAO and STO bulk single crystals with similar ABO_3 structures. Such a notably low thermal conductivity of LCO at room temperature is consistent with literature reports, and has been attributed to the spin-state transition of thermally-excited Co ions from the low spin to finite spin states. This crossover is complete by ~100 K, leading to an equal population, in a simple picture, of low spin and finite spin states, accompanied by subsequent bond-length fluctuations, which significantly suppress the thermal conductivity.[53-54] With the increase of Sr doping (x), this suppression of 300 K $La_{1-x}Sr_xCoO_3$ thermal conductivity due to the thermally-excited spin-state transition becomes less influential and essentially negligible when $x > 0.18$, where the scattering of phonons by Sr dopants becomes dominant.[53] Since the samples studied in this work are at $x = 0.3$ or 0.5, and are in the ferromagnetic metallic phase (with the exception of the 3 nm LSCO film on STO where dead layer effects induce a non-ferromagnetic semiconducting ground state[32]), this excludes the spin-state transition, or other magnetic/electronic effects as a dominant reason for the thermal conductivity suppression in LSCO epitaxial films. Again, the thermal conductivity is ~1.7 W m^{-1} K^{-1} for LSCO epitaxial thin films on both substrates, close to that of amorphous SiO_2 (1.3–1.4 W m^{-1} K^{-1}), and is independent of the ordering of oxygen vacancy planes. The close-to-amorphous-limit Λ_{LSCO} suggests that phonon transport is somehow suppressed by ~60% in LSCO epitaxial thin films, which we investigate below.

Table II. Lattice thermal conductivities of single-crystal $La_{1-x}Sr_xCoO_{3-\delta}$, $LaAlO_3$, and $SrTiO_3$ from both TDTR measurements (Λ_{meas}) and BTE calculation (Λ_{cal}).

	ABO_3	$La_{0.7}Sr_{0.3}CoO_3$	$LaCoO_{2.9}$	$La_{0.7}Sr_{0.3}CoO_{2.9}$	$La_{0.5}Sr_{0.5}CoO_{2.9}$			
h (nm)	Bulk				Bulk	18	6	3
Λ_{meas} ($W\ m^{-1}\ K^{-1}$)	2.2 ($LaCoO_3$)[a] 13 ($LaAlO_3$) 11 ($SrTiO_3$)	6.2	N/A	N/A		1.7 (avg)[b]		
Λ_{cal} ($W\ m^{-1}\ K^{-1}$)	~12–15	8.7	4.4	6.0	5.6	1.54	1.04	0.81

[a] The spin-state transition effect in LCO randomly tilts the octahedral locally, thus reducing the thermal conductivity of LCO from the perfect lattice value 12~15 to the real lattice value 2.2. Since this spin-state transition effect does not exist in these LSCO samples, we do not consider it in our modeling (see main text for a more detailed explanation).[53-54]

[b] The measured thermal conductivity of 1.7 $W\ m^{-1}\ K^{-1}$ is averaged over $La_{0.5}Sr_{0.5}CoO_{2.9}$ epitaxial films of 6 - 18 nm.

4.3. Impacts of Sr Substitution, Oxygen Vacancies, and Boundary Scattering

We now systematically evaluate the possible contributions of La/Sr mass disorder, oxygen vacancies, and boundary scattering (size effects) on the lattice thermal conductivity of LSCO using the BTE model (Section S2 of the Supporting Information). The calculated lattice thermal conductivities are listed in Table II.

In the BTE model, both La/Sr mass disorder (resulting from Sr substitution) and oxygen vacancies are treated as point defects. The phonon scattering rates induced by these two types of point defects share the same form of expression, but involve different scattering coefficients (g), which describes the strength of phonon scattering with different types of point defects (Section S2 of the Supporting Information). For the La/Sr mass disorder in LSCO with $x = 0.3$, g_{Sr} is calculated to be 0.036. For oxygen vacancies at a level of $\delta = 0.1$, the mass disorder associated with the removal of oxygen ions (g_{Ov}) will be magnified by a factor of three to take into account the potential energy change due to the missing bond.[89] This leads to g_{Ov} = 0.11, nearly three times that of g_{Sr}. With these scattering coefficients, the calculated Λ_{LSCO} according to the Matthiessen rule expressed by Eq. (3) is 8.7 W m^{-1} K^{-1} for the La/Sr mass disorder at $x = 0.3$ ($La_{0.7}Sr_{0.3}CoO_3$), decreased by 42% in comparison to that of a perfectly stoichiometric ABO_3 structure (15 W m^{-1} K^{-1}). We emphasize that the BTE calculation used here can only compare the relative contributions of phonon scattering by point defects (i.e., the La/Sr mass disorder and oxygen vacancies) and boundaries, as it does not take into account the spin-state transition. Thus, the BTE calculation predicts a similar thermal conductivity for the stoichiometric structure of ABO_3 for all three single crystals of LAO, STO, and LCO, which indeed agrees reasonably well with the measured thermal conductivities of LAO and STO, which are not subject to the spin-state transition effect.

For LCO single crystals with $\delta = 0.1$, only ~3% oxygen vacancies will decrease the thermal conductivity of $LaCoO_{2.9}$ to 4.4 W m^{-1} K^{-1}, providing more suppression of phonon heat transport than ~30% Sr substitution for La (in $La_{0.7}Sr_{0.3}CoO_3$). These results from BTE modeling thus indicate that oxygen vacancy formation (δ) has a significantly larger impact on the phonon scattering rate than La/Sr mass disorder (x), and is thus the dominant factor for Λ_{LSCO} reduction. This observation is consistent with the trends of thermal conductivities obtained from both TDTR measurements and MD simulations discussed later.

To study the boundary scattering effect on the thermal transport in LSCO epitaxial films due to their finite thicknesses, we plot the cumulative thermal conductivity Λ_{cumu} as a function of the phonon MFP, and thermal conductivity Λ_{LSCO} as a function of thickness h_{LSCO} for $La_{0.5}Sr_{0.5}CoO_{2.9}$ in Fig. 5. For bulk single crystals of LSCO, with no size limitations, heat-carrying phonons with all MFPs contribute to the thermal transport, corresponding to

Λ_{LSCO} = 5.6 W m^{-1} K^{-1} for bulk $La_{0.5}Sr_{0.5}CoO_{2.9}$ in Table II. The enhanced boundary scattering of phonons resulting from the low layer thickness decreases Λ_{LSCO} from 1.54 to 1.04 W m^{-1} K^{-1} when the layer thickness changes from 18 to 6 nm, as shown in the inset plot of Λ_{LSCO} vs. h_{LSCO} from 0 to 18 nm. As can be seen, the dependence of Λ_{LSCO} on h_{LSCO} is relatively weak over the range 6-18 nm. This justifies our approach of using a linear extrapolation of R_{eff} to extract the thickness-independent Λ_{LSCO} from TDTR. The average Λ_{LSCO} (assuming Λ_{LSCO} has a linear relationship with h_{LSCO}) is calculated to be 1.3 W m^{-1} K^{-1} for LSCO epitaxial films of 6-18 nm, which is in very reasonable agreement (~24% deviation) with the value of 1.7 W m^{-1} K^{-1} obtained from measurements.

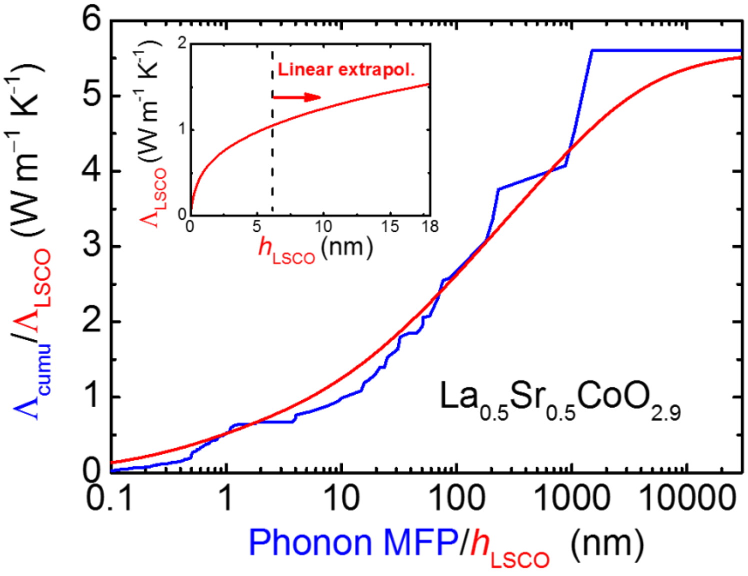

Figure 5. Cumulative thermal conductivity Λ_{cumu} as a function of phonon MFP (blue line) and thermal conductivity Λ_{LSCO} as a function of film thickness h_{LSCO} (red line) from the BTE calculation for $La_{0.5}Sr_{0.5}CoO_{2.9}$ crystals. The inset plot is the detailed Λ_{LSCO} in the thickness range of 0 to 18 nm.

While the above significantly elucidates the dependence on the concentration of oxygen vacancies, their ordering cannot be captured by BTE calculations. We thus performed MD simulations to better understand the effect of OVO on the thermal conductivity of LSCO, and to cross-check the BTE results regarding the dependence of Λ_{LSCO} on x and δ. The thermal conductivity of 8 specific cases calculated by MD simulations are presented in Fig. 6. From left to right we show the thermal conductivities of (1) Cases 1-4 consisting of $La_{1-x}Sr_xCoO_{3-\delta}$ with varying x (from 0 to 0.5) and no oxygen vacancies ($\delta = 0$); (2) Cases 5 and 6 corresponding to $La_{1-x}Sr_xCoO_{3-\delta}$ with $x = 0.3$, 0.5 and $\delta \approx 0.1$, in which the oxygen vacancies are randomly distributed; and (3) Cases 7 and 8 representing $La_{1-x}Sr_xCoO_{3-\delta}$ with $x = 0.5$, and $\delta = 0.1$ and 0.5, in which oxygen vacancies exhibit horizontal ordering (as for the LSCO epitaxial film on the LAO substrate). The oxygen vacancy distribution for case 7 represents as closely as possible the real LSCO epitaxial films ($x = 0.5$ and $\delta \approx 0.1$) as characterized by STEM/EELS (Section 4.1 above). The structure of case 7 in these MD simulations was created by randomly adding oxygen ions back to the vacancy sites along the periodic <110> oxygen vacancy lines, per the perfect ordering of oxygen vacancies (case 8, $x = 0.5$ and $\delta = 0.5$) depicted in the schematic of the LSCO epitaxial film on LAO (Section 4.1). In cases 7 and 8, Λ_{ab} and Λ_c are the in-plane and through-plane thermal conductivities, respectively, corresponding to thermal conductivities along the directions parallel and perpendicular to the horizontal ordering of OVO planes. Due to the identical structures, the in-plane thermal conductivity of Λ_{ab} for case 7, with the horizontal OVO, can be treated as the through-plane thermal conductivity of LSCO with vertical OVO. Such an approximation enables the comparison of Λ_{ab} and Λ_c predicted by MD with the measured through-plane thermal conductivities of LSCO epitaxial films with both the horizontal (sample A) and vertical (sample B) oxygen vacancy ordering.

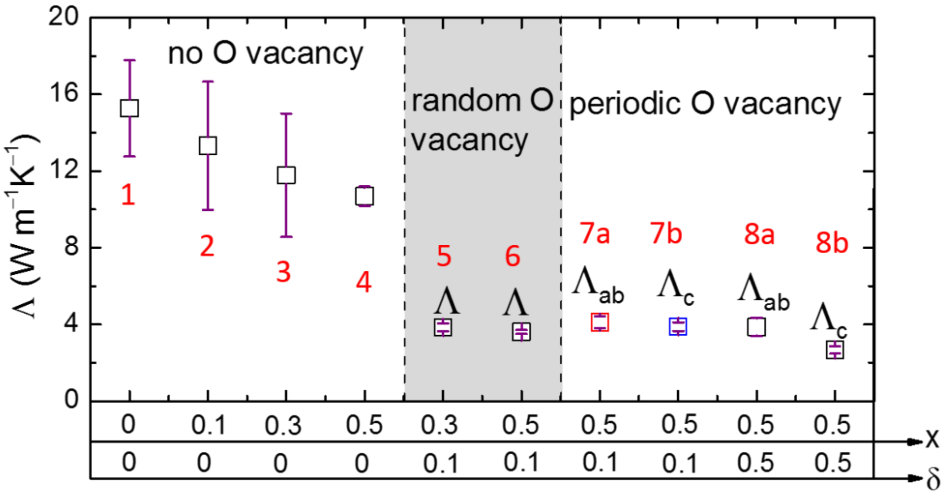

Figure 6. Summary of the thermal conductivities of LSCO as functions of x and δ from MD simulations. Λ_{ab} and Λ_c denote the thermal conductivities of the LSCO epitaxial thin films along the in-plane and through-plane directions, respectively. The left columns (cases 1-4) are the results for $La_{1-x}Sr_xCoO_{3-\delta}$ with $x = 0$~0.5 and no oxygen vacancies ($\delta = 0$). The middle columns (case 5 and 6) correspond to the sample case of $La_{1-x}Sr_xCoO_{3-\delta}$ with $x = 0.3$, 0.5 and $\delta \approx 0.1$, in which the oxygen vacancy are randomly distributed. The right columns (cases 7 and 8) are the results of $La_{1-x}Sr_xCoO_{3-\delta}$ with $x = 0.5$ and $\delta = 0.1$ and 0.5, in which oxygen vacancies exhibit horizontal ordering and periodic distribution created by removing the oxygen atoms along the <110> periodic lines.

According to the MD results, increasing x from 0 to 0.5 only reduces the thermal conductivity of LSCO by 27% from 15 (case 1) to 11 W m^{-1} K^{-1} (case 4), while the increase of δ from 0 to 0.1 reduces the thermal conductivity of LSCO by 67% from 12 (case 3) to ~4 W m^{-1} K^{-1} (cases 5 and 7). Λ_{LSCO} also does not change much upon increasing x from 0.3 (case 5) to 0.5 in samples with $\delta = 0.1$ (cases 6 and 7), where its reduction is already sufficiently large. These results suggest that, overall, the effect of oxygen vacancy density on reducing the thermal conductivity of LSCO is substantially stronger than Sr substitution. Additionally, when the oxygen vacancy density is sufficiently large ($\delta > 0.1$), further increase of δ leads to negligible additional reduction of Λ_{LSCO}.

The impact of oxygen vacancy ordering on the thermal transport in LSCO can be examined by inspecting the in-plane and through-plane thermal conductivities of case 7 ($x = 0.5$ and $\delta = 0.1$). The MD prediction shows $\Lambda_{ab} = 4.1 \pm 0.30$ W m^{-1} K^{-1} and $\Lambda_c = 3.9 \pm 0.23$ W m^{-1} K^{-1}, leading to a negligibly small anisotropy (~5%) in the in-plane and through-plane thermal transport. This agrees with our TDTR observations that the through-plane thermal conductivity is ~1.7 W m^{-1} K^{-1} for LSCO epitaxial films on both LAO and STO substrates, regardless of the ordering of the oxygen vacancies. We speculate that while the thermal conductivity of LSCO epitaxial films can be significantly reduced by the oxygen vacancy and size effects, the relatively small density of $\delta = 0.1$ is not sufficient to preserve the perfection of ordering of oxygen vacancy planes that would be necessary for highly anisotropic thermal transport. When δ is high, the anisotropy induced by the ordering of oxygen vacancy planes is more pronounced. In case 8 with $\delta = 0.5$, the OVO planes are perfectly controlled with all the oxygen removal along <110> vacancy lines, such that the anisotropy of thermal conductivity of the LSCO films is increased to 35%. On the other hand, a high δ will also produce larger reduction in thermal conductivity, which further constrains the MFPs of dominant heat carriers, and subsequently suppresses thermal anisotropy. The above mechanisms for high δ samples essentially represent two competing effects on the thermal anisotropy.

4.4. Electronic Thermal Conductivity of LSCO Epitaxial Thin Films - Electron/Phonon Coupling

The above analysis of LSCO thermal transport focuses on the lattice (phonon) contributions. To estimate the electronic contribution to the overall thermal conductivity of LSCO epitaxial films, we applied the van der Pauw method to obtain the electrical conductivity/resistivity along the in-plane direction (Fig. 7a). While much greater at low temperatures, at 300 K the electrical resistivities exhibit around a factor of two difference in LSCO films with different orientations of ordering of the oxygen vacancy planes. For example, the resistivities are 210 and 400 μΩcm for Type A and B samples of 12.5-nm thick films at 300 K, respectively, which results in an in-plane electronic thermal conductivity ($\Lambda_{\text{el\_in}}$) of sample A (LSCO on LAO with horizontal OVO planes) that is two times larger than those for sample B (LSCO on STO with vertical OVO planes).

The ultralow thickness of LSCO epitaxial films leads to the low measurement sensitivity to the LSCO in-plane thermal conductivity[76,90], in addition to the challenge of probing the through-plane electrical conductivity. Thus, for the LSCO epitaxial films in this work, we are unable to directly compare the electronic and phononic contributions to the total thermal conductivity along the same direction for electrical and thermal characterization. However, to a first approximation, we can make a qualitative discussion by comparing the through-plane thermal conductivity (Λ_{LSCO}) with certain assumptions. We first assume that the anisotropy of the electric conductivity (σ) in LSCO epitaxial films is approximately the ratio of the in-plane σ of LSCO on LAO to that of LSCO on STO (a factor of two). In addition to this, the MD simulations discussed in Section 4.3 demonstrate that the phononic thermal transport is isotropic in these LSCO epitaxial films. When combined, the overall thermal transport consisting of both the electronic and phononic contributions should reflect the electronic thermal anisotropy along the through-plane direction in these LSCO films with different OVO planes. However, TDTR experimental observations show that Λ_{LSCO} is almost the same for LSCO epitaxial films with both the vertical and horizontal oxygen vacancy orderings. This indicates that the electronic contribution to the thermal conductivity has not been captured by TDTR measurements along the through-plane direction.

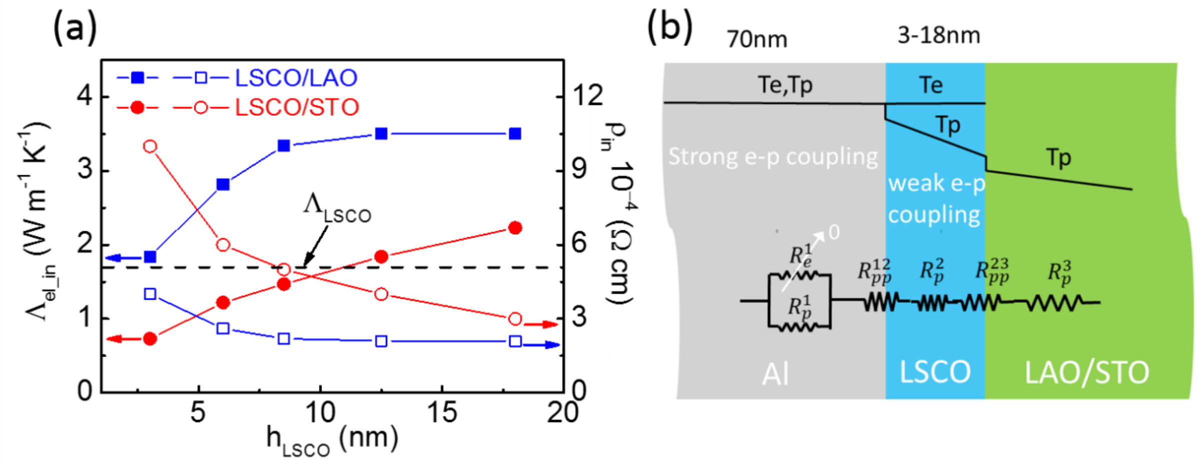

Figure 7. (a) In-plane electronic thermal conductivity of LSCO thin films (Λ_{el_in}) as a function of thickness, converted from the Wiedemann-Franz law for LSCO films with horizontal (blue) and vertical (red) ordering of the oxygen vacancy planes. The through-plane thermal conductivity of LSCO thin films (Λ_{LSCO}) extracted from the thickness-dependent TDTR measurements is also plotted for comparison (black dashed line). (b) Schematic of thermal resistances consisting of electron-phonon coupling in the Al transducer layer and the metallic LSCO epitaxial film. Heat is predominantly carried by phonons in the LSCO epitaxial film due to its ultralow thickness which confines the electron cooling length.

We hypothesize two possible reasons for the experimental observation that the electronic contribution to the thermal transport is not detectable in TDTR: (1) The LAO and STO substrates in this work are electrically insulating materials. This leads to the fact that heat carried by electrons in LSCO epitaxial films cannot dissipate directly into the electrically insulating substrate *via* electron transport at the LSCO/substrate interface. Therefore, an adiabatic boundary condition for electronic thermal transport at this LSCO/substrate interface should be considered, and, accordingly, a confinement of the electron cooling length occurs in these ultrathin films; (2) We also speculate that the electron-phonon coupling within the LSCO epitaxial films is relatively weak, such that electrons cannot deposit their thermal energy to phonons in the LSCO films. With the two aspects mentioned above, the electron temperature gradient along the through-plane direction will be rather flat and the contributions from electronic transport to the measured overall Λ_{LSCO} will be suppressed.

5. CONCLUSIONS

We have reported the through-plane thermal conductivities of $La_{0.5}Sr_{0.5}CoO_{2.9}$ epitaxial thin films (6 to 18 nm thickness) deposited on both LAO and STO substrates to be 1.7 W m^{-1} K^{-1}, suppressed by 70% compared to bulk single crystal LSCO (6.2 W m^{-1} K^{-1}). This is close to the limit of amorphous oxides (*e.g.* 1.3 W m^{-1} K^{-1} for amorphous SiO_2). Oxygen vacancy ordering (horizontal and vertical to the in-plane direction) has negligible effect on the thermal conductivity of these materials. Such features are mainly attributed to point defects of oxygen vacancies and Sr substitution, the size effect resulting from the ultralow film thickness, and weak electron/phonon coupling within the LSCO film. BTE modeling and MD simulation of the thermal transport across the LSCO epitaxial film separately elucidates the effects of Sr substitution, oxygen vacancies, boundary scattering (the size effect), and oxygen vacancy ordering. The results indicate that oxygen vacancies have a much stronger effect than La/Sr mass disorder on the suppression of thermal conductivity in LSCO epitaxial films, which explains the extremely low thermal conductivity of the LSCO epitaxial films with oxygen vacancies observed in TDTR measurements. The cumulative thermal conductivity of LSCO epitaxial thin films are also obtained, and the averaged values of Λ_{LSCO} within the thickness range of the LSCO thin-film samples are comparable to experimental values. From this we find that the close-to-amorphous limit of thermal conductivity is partially due to the truncation of phonons with MFPs larger than the film thickness. Moreover, MD simulation validates that the OVO effect on thermal conductivity of LSCO is negligible when $\delta = 0.1$. The ultralow thickness (~ tens of nanometers) and weak electron/phonon coupling of the LSCO epitaxial films also confine the electronic cooling length and suppress the electronic contribution to the overall thermal conductivity. The structure-thermal property correlations revealed in this study open up possibilities for tuning the thermal properties of perovskite thin films by manipulating heat carriers *via* structural/defect engineering at the atomic level. In addition, the results from this work can facilitate potential thermal applications of perovskite oxides, particularly as the building blocks for device fabrication and performance optimization in thermoelectric and thermal barrier materials.

ASSOCIATED CONTENT

The Supporting Information is available free of charge on the ACS Publication website.

ACKNOWLEDGMENTS

This work is supported by the National Science Foundation (NSF) through the University of Minnesota MRSEC under Award Number DMR-1420013 (X. W. W., X. J. W., J. W., and C. L.), T.F. and X.R. acknowledge the support from National Science Foundation (Award No. 1150948), J.Z. would like to thank the support from the National Natural Science Foundation of China (Grant No. 51336009 and No. 51373184). Work at Argonne National Laboratory (crystal growth and characterization) was sponsored by the U.S. Department of Energy, Office of Science, Basic

Energy Sciences, Materials Science and Engineering Division. Research at UCM sponsored by Spanish MINECO/FEDER MAT2015-66888-C3-3-R and by the ERC Proof of Concept Grant MAGTOOLS. Electron microscopy work at ORNL was sponsored by the Materials Sciences and Engineering Division of the U.S. Department of Energy and ORNL's Center for Nanophase Materials User Program.

REFERENCES

(1) Dagotto, E. Correlated Electrons in High-Temperature Superconductors. *Rev. Mod. Phys.* **1994,** *66* (3), 763.

(2) Haertling, G. H. Ferroelectric Ceramics: History and Technology. *J. Am. Ceram. Soc.* **1999,** *82* (4), 797-818.

(3) Cohen, R. E. Origin of Ferroelectricity in Perovskite Oxides. *Nature* **1992,** *358* (6382), 136-138.

(4) Ravichandran, J.; Siemons, W.; Oh, D.-W.; Kardel, J. T.; Chari, A.; Heijmerikx, H.; Scullin, M. L.; Majumdar, A.; Ramesh, R.; Cahill, D. G. High-Temperature Thermoelectric Response of Double-Doped $SrTiO_3$ Epitaxial Films. *Phys. Rev. B* **2010,** *82* (16), 165126.

(5) Wang, H.; Su, W.; Liu, J.; Wang, C. Recent Development of n-Type Perovskite Thermoelectrics. *J. Materiomics* **2016,** *2* (3), 225-236.

(6) Kharton, V.; Viskup, A.; Naumovich, E.; Lapchuk, N. Mixed Electronic and Ionic Conductivity of $LaCo(M)O_3$ (M = Ga, Cr, Fe or Ni): I. Oxygen Transport in Perovskites $LaCoO_3$–$LaGaO_3$. *Solid State Ionics* **1997,** *104* (1), 67-78.

(7) Coey, J.; Viret, M.; Von Molnar, S. Mixed-Valence Manganites. *Adv. Phys.* **2009,** *58* (6), 571-697.

(8) Jun, A.; Kim, J.; Shin, J.; Kim, G. Perovskite as a Cathode Material: A Review of Its Role in Solid-Oxide Fuel Cell Technology. *ChemElectroChem* **2016,** *3* (4), 511-530.

(9) Maeno, Y.; Hashimoto, H.; Yoshida, K.; Nishizaki, S.; Fujita, T.; Bednorz, J.; Lichtenberg, F. Superconductivity in a Layered Perovskite without Copper. *Nature* **1994,** *372* (6506), 532-534.

(10) Cava, R.; Batlogg, B.; Van Dover, R.; Murphy, D.; Sunshine, S.; Siegrist, T.; Remeika, J.; Rietman, E.; Zahurak, S.; Espinosa, G. Bulk Superconductivity at 91 K in Single-Phase Oxygen-Deficient Perovskite $Ba_2YCu_3O_{9-\delta}$. *Phys. Rev. Lett.* **1987,** *58* (16), 1676.

(11) Sawa, A. Resistive Switching in Transition Metal Oxides. *Mater. Today* **2008,** *11* (6), 28-36.

(12) Flahaut, D.; Mihara, T.; Funahashi, R.; Nabeshima, N.; Lee, K.; Ohta, H.; Koumoto, K. Thermoelectrical Properties of A-Site Substituted $Ca_{1-x}Re_xMnO_3$ System. *J. Appl. Phys.* **2006,** *100* (8), 084911-084911.

(13) Ohta, S.; Nomura, T.; Ohta, H.; Hirano, M.; Hosono, H.; Koumoto, K. Large Thermoelectric Performance of Heavily Nb-Doped $SrTiO_3$ Epitaxial Film at High Temperature. *Appl. Phys. Lett.* **2005,** *87* (9), 092108.

(14) Snyder, G. J.; Toberer, E. S. Complex Thermoelectric Materials. *Nat. Mater.* **2008,** *7* (2), 105-114.

(15) Dimos, D.; Mueller, C. Perovskite Thin Films for High-Frequency Capacitor Applications 1. *Annu. Rev. Mater. Sci.* **1998,** *28* (1), 397-419.

(16) Ramesh, R.; Spaldin, N. A. Multiferroics: Progress and Prospects in Thin Films. *Nat. Mater.* **2007,** *6* (1), 21-29.

(17) Fuchs, D.; Schneider, C.; Schneider, R.; Rietschel, H. High Dielectric Constant and Tunability of Epitaxial $SrTiO_3$ Thin Film Capacitors. *J. Appl. Phys.* **1999,** *85* (10), 7362-7369.

(18) Wu, J.; Leighton, C. Glassy Ferromagnetism and Magnetic Phase Separation in $La_{1-x}Sr_xCoO_3$. *Phys. Rev. B* **2003,** *67* (17), 174408.

(19) Raccah, P.; Goodenough, J. A Localized-Electron to Collective-Electron Transition in the System (La, Sr)CoO_3. *J. Appl. Phys.* **1968,** *39* (2), 1209-1210.

(20) Teraoka, Y.; Zhang, H.-M.; Furukawa, S.; Yamazoe, N. Oxygen Permeation through Perovskite-Type Oxides. *Chem. Lett.* **1985,** *14* (11), 1743-1746.

(21) Liu, W.; Wang, S.; Chen, Y.; Fang, G.; Li, M.; Zhao, X.-z. $La_{0.5}Sr_{0.5}CoO_{3-\delta}$ Nanotubes Sensor for Room Temperature Detection of Ammonia. *Sensor Actuat. B-Chem.* **2008,** *134* (1), 62-65.

(22) Wang, S.; Kato, T.; Nagata, S.; Honda, T.; Kaneko, T.; Iwashita, N.; Dokiya, M. Performance of a $La_{0.6}Sr_{0.4}Co_{0.8}Fe_{0.2}O_3$-$Ce_{0.8}Gd_{0.2}O_{1.9}$-Ag Cathode for Ceria Electrolyte SOFCs. *Solid State Ionics* **2002,** *146* (3), 203-210.

(23) Jonker, G.; Van Santen, J. Magnetic Compounds with Perovskite Structure III. Ferromagnetic Compounds of Cobalt. *Physica* **1953,** *19* (1), 120-130.

(24) Long, Y.; Kaneko, Y.; Ishiwata, S.; Taguchi, Y.; Tokura, Y. Synthesis of Cubic $SrCoO_3$ Single Crystal and Its Anisotropic Magnetic and Transport Properties. *J. Phys.: Condens. Matter* **2011,** *23* (24), 245601.

(25) Klie, R.; Ito, Y.; Stemmer, S.; Browning, N. Observation of Oxygen Vacancy Ordering and Segregation in Perovskite Oxides. *Ultramicroscopy* **2001,** *86* (3), 289-302.

(26) Ito, Y.; Klie, R. F.; Browning, N. D.; Mazanec, T. J. Atomic Resolution Analysis of the Defect Chemistry and Microdomain Structure of Brownmillerite-Type Strontium Cobaltite. *J. Am. Ceram. Soc.* **2002,** *85* (4), 969-976.

(27) Xie, C.; Nie, Y.; Wells, B.; Budnick, J.; Hines, W.; Dabrowski, B. Magnetic Phase Separation in $SrCoO_x$ ($2.5 \leqslant x \leqslant 3$). *Appl. Phys. Lett.* **2011,** *99* (5), 052503.

(28) Jeen, H.; Choi, W. S.; Biegalski, M. D.; Folkman, C. M.; Tung, I.-C.; Fong, D. D.; Freeland, J. W.; Shin, D.; Ohta, H.; Chisholm, M. F.; Lee, H. N. Reversible Redox Reactions in an Epitaxially Stabilized $SrCoO_x$ Oxygen Sponge. *Nat. Mater.* **2013,** *12* (11), 1057-1063.

(29) Jeen, H.; Choi, W. S.; Freeland, J. W.; Ohta, H.; Jung, C. U.; Lee, H. N. Topotactic Phase Transformation of the Brownmillerite $SrCoO_{2.5}$ to the Perovskite $SrCoO_{3-\delta}$. *Adv. Mater.* **2013,** *25* (27), 3651-3656.

(30) Petrie, J. R.; Mitra, C.; Jeen, H.; Choi, W. S.; Meyer, T. L.; Reboredo, F. A.; Freeland, J. W.; Eres, G.; Lee, H. N. Strain Control of Oxygen Vacancies in Epitaxial Strontium Cobaltite Films. *Adv. Funct. Mater.* **2016,** *26* (10), 1564-1570.

(31) Gazquez, J.; Bose, S.; Sharma, M.; Torija, M. A.; Pennycook, S. J.; Leighton, C.; Varela, M. Lattice Mismatch Accommodation via Oxygen Vacancy Ordering in Epitaxial $La_{0.5}Sr_{0.5}CoO_{3-\delta}$ Thin Films. *APL Mater.* **2013,** *1* (1), 012105.

(32) Torija, M. A.; Sharma, M.; Gazquez, J.; Varela, M.; He, C.; Schmitt, J.; Borchers, J. A.; Laver, M.; El-Khatib, S.; Leighton, C. Chemically Driven Nanoscopic Magnetic Phase Separation at the $SrTiO_3$(001)/$La_{1-x}Sr_xCoO_3$ Interface. *Adv. Mater.* **2011,** *23* (24), 2711-2715.

(33) Torija, M. A.; Sharma, M.; Fitzsimmons, M. R.; Varela, M.; Leighton, C. Epitaxial $La_{0.5}Sr_{0.5}CoO_3$ Thin Films: Structure, Magnetism, and Transport. *J. Appl. Phys.* **2008,** *104* (2), 023901.

(34) Klenov, D. O.; Donner, W.; Foran, B.; Stemmer, S. Impact of Stress on Oxygen Vacancy Ordering in Epitaxial $(La_{0.5}Sr_{0.5})CoO_{3-\delta}$ Thin Films. *Appl. Phys. Lett.* **2003,** *82* (20), 3427-3429.

(35) Wang, Z.; Yin, J.; Jiang, Y. EELS Analysis of Cation Valence States and Oxygen Vacancies in Magnetic Oxides. *Micron* **2000,** *31* (5), 571-580.

(36) Wang, Z. L.; Zhang, J. Tetragonal Domain Structure and Magnetoresistance of $La_{1-x}Sr_xCoO_3$. *Phys. Rev. B* **1996,** *54* (2), 1153.

(37) Vassen, R.; Cao, X.; Tietz, F.; Basu, D.; Stöver, D. Zirconates as New Materials for Thermal Barrier Coatings. *J. Am. Ceram. Soc.* **2000,** *83* (8), 2023-2028.

(38) Brooks, C. M.; Wilson, R. B.; Schäfer, A.; Mundy, J. A.; Holtz, M. E.; Muller, D. A.; Schubert, J.; Cahill, D. G.; Schlom, D. G. Tuning Thermal Conductivity in Homoepitaxial $SrTiO_3$ Films via Defects. *Appl. Phys. Lett.* **2015,** *107* (5), 051902.

(39) Fergus, J. W. Oxide Materials for High Temperature Thermoelectric Energy Conversion. *J. Eur. Ceram. Soc.* **2012,** *32* (3), 525-540.

(40) Weidenkaff, A.; Robert, R.; Aguirre, M.; Bocher, L.; Lippert, T.; Canulescu, S. Development of Thermoelectric Oxides for Renewable Energy Conversion Technologies. *Renew. Energy* **2008,** *33* (2), 342-347.

(41) Jha, P.; Sands, T. D.; Cassels, L.; Jackson, P.; Favaloro, T.; Kirk, B.; Zide, J.; Xu, X.; Shakouri, A. Cross-Plane Electronic and Thermal Transport Properties of p-Type $La_{0.67}Sr_{0.33}MnO_3$/$LaMnO_3$ Perovskite Oxide Metal/Semiconductor Superlattices. *J. Appl. Phys.* **2012,** *112* (6), 063714.

(42) Cheung, J. T.; Morgan, P. E.; Lowndes, D. H.; Zheng, X. Y.; Breen, J. Structural and Electrical Properties of $La_{0.5}Sr_{0.5}CoO_3$ Epitaxial Films. *Appl. Phys. Lett.* **1993,** *62* (17), 2045-2047.

(43) Luo, G. P.; Wang, Y. S.; Chen, S. Y.; Heilman, A. K.; Chen, C. L.; Chu, C. W.; Liou, Y.; Ming, N. B. Electrical and Magnetic Properties of $La_{0.5}Sr_{0.5}CoO_3$ Thin Films. *Appl. Phys. Lett.* **2000,** *76* (14), 1908-1910.

(44) Rata, A.; Herklotz, A.; Nenkov, K.; Schultz, L.; Dörr, K. Strain-Induced Insulator State and Giant Gauge Factor of $La_{0.7}Sr_{0.3}CoO_3$ Films. *Phys. Rev. Lett.* **2008,** *100* (7), 076401.

(45) Othmen, Z.; Schulman, A.; Daoudi, K.; Boudard, M.; Acha, C.; Roussel, H.; Oueslati, M.; Tsuchiya, T. Structural, Electrical and Magnetic Properties of Epitaxial $La_{0.7}Sr_{0.3}CoO_3$ Thin Films Grown on $SrTiO_3$ and $LaAlO_3$ Substrates. *Appl. Surf. Sci.* **2014,** *306*, 60-65.

(46) Varela, M.; Salafranca, J.; Biskup, N.; Gazquez, J.; Oxley, M.; Mehta, V.; Suzuki, Y.; Bose, S.; Sharma, M.; Leighton, C. Oxygen Vacancy Ordering: a Degree of Freedom that can Control the Structural, Electronic and Magnetic Properties of Transition-Metal Oxide Films. *Microsc. Microanal.* **2014,** *20* (S3), 556-557.

(47) Chen, X.; Wang, S.; Yang, Y.; Smith, L.; Wu, N.; Kim, B.-I.; Perry, S.; Jacobson, A.; Ignatiev, A. Electrical Conductivity Relaxation Studies of an Epitaxial $La_{0.5}Sr_{0.5}CoO_{3-\delta}$ Thin Film. *Solid State Ionics* **2002,** *146* (3), 405-413.

(48) Kelly, S.; Galli, F.; Aarts, J.; Bose, S.; Sharma, M.; Leighton, C. Direct Real Space Observation of Magneto-Electronic Inhomogeneity in Ultra-Thin Film $La_{0.5}Sr_{0.5}CoO_{3-\delta}$ on $SrTiO_3$(001). *Appl. Phys. Lett.* **2014,** *105* (11), 112909.

(49) Donner, W.; Chen, C.; Liu, M.; Jacobson, A. J.; Lee, Y.-L.; Gadre, M.; Morgan, D. Epitaxial Strain-Induced Chemical Ordering in $La_{0.5}Sr_{0.5}CoO_{3-\delta}$ Films on $SrTiO_3$. *Chem. Mater.* **2011,** *23* (4), 984-988.

(50) Woicik, J. C.; Xie, C. K.; Wells, B. O. Effect of Strain on the Local Perovskite Structure: $La_{0.5}Sr_{0.5}CoO_3$. *J. Appl. Phys.* **2011,** *109* (8), 083519.

(51) Gazquez, J.; Luo, W.; Oxley, M. P.; Prange, M.; Torija, M. A.; Sharma, M.; Leighton, C.; Pantelides, S. T.; Pennycook, S. J.; Varela, M. Atomic-Resolution Imaging of Spin-State Superlattices in Nanopockets within Cobaltite Thin Films. *Nano Lett.* **2011,** *11* (3), 973-976.

(52) Biegalski, M.; Takamura, Y.; Mehta, A.; Gai, Z.; Kalinin, S. V.; Ambaye, H.; Lauter, V.; Fong, D.; Pantelides, S. T.; Kim, Y. Interrelation between Structure-Magnetic Properties in $La_{0.5}Sr_{0.5}CoO_3$. *Adv. Mater. Inter.* **2014,** *1* (8), 1400203.

(53) Berggold, K.; Kriener, M.; Zobel, C.; Reichl, A.; Reuther, M.; Müller, R.; Freimuth, A.; Lorenz, T. Thermal Conductivity, Thermopower, and Figure of Merit of $La_{1-x}Sr_xCoO_3$. *Phys. Rev. B* **2005,** *72* (15), 155116.

(54) Yan, J.-Q.; Zhou, J.-S.; Goodenough, J. Bond-Length Fluctuations and the Spin-State Transition in $LCoO_3$ (L= La, Pr, and Nd). *Phys. Rev. B* **2004,** *69* (13), 134409.

(55) Kashiwada, Y.; Fujishiro, H.; Fujine, Y.; Ikebe, M.; Hejtmanek, J. Metal–Insulator Transition and Phonon Scattering Mechanisms in $La_{1-x}Sr_xCoO_3$. *Physica B: Condensed Matter.* **2006,** *378,* 529-531.

(56) Wang, Y.; Li, F.; Xu, L.; Sui, Y.; Wang, X.; Su, W.; Liu, X. Large Thermal Conductivity Reduction Induced by La/O Vacancies in the Thermoelectric $LaCoO_3$ System. *Inorg. Chem.* **2011,** *50* (10), 4412-4416.

(57) Zhou, A.; Zhu, T.; Zhao, X. Thermoelectric Properties of Perovskite-Type Oxide $La_{1-x}Sr_xCoO_3$ (x=0, 0.1) Prepared by Solid State Reactions. *Mater. Sci. Eng. B-Adv.* **2006,** *128* (1), 174-178.

(58) Durá, O.; Rogl, P.; Falmbigl, M.; Hilscher, G.; Bauer, E. Thermoelectric and Magnetic Properties of Nanocrystalline $La_{0.7}Sr_{0.3}CoO_3$. *J. Appl. Phys.* **2012,** *111* (6), 063722.

(59) Oh, D.-W.; Ravichandran, J.; Liang, C.-W.; Siemons, W.; Jalan, B.; Brooks, C. M.; Huijben, M.; Schlom, D. G.; Stemmer, S.; Martin, L. W. Thermal Conductivity as a Metric for the Crystalline Quality of $SrTiO_3$ Epitaxial Layers. *Appl. Phys. Lett.* **2011,** *98* (22), 221904.

(60) Breckenfeld, E.; Wilson, R.; Karthik, J.; Damodaran, A.; Cahill, D.; Martin, L. Effect of Growth Induced (Non) Stoichiometry on the Structure, Dielectric Response, and Thermal Conductivity of $SrTiO_3$ Thin Films. *Chem. Mater.* **2012,** *24* (2), 331-337.

(61) Foley, B. M.; Brown-Shaklee, H. J.; Duda, J. C.; Cheaito, R.; Gibbons, B. J.; Medlin, D.; Ihlefeld, J. F.; Hopkins, P. E. Thermal Conductivity of Nano-Grained $SrTiO_3$ Thin Films. *Appl. Phys. Lett.* **2012,** *101* (23), 231908.

(62) Yu, C.; Scullin, M. L.; Huijben, M.; Ramesh, R.; Majumdar, A. Thermal Conductivity Reduction in Oxygen-Deficient Strontium Titanates. *Appl. Phys. Lett.* **2008,** *92* (19), 191911.

(63) Zhu, J.; Tang, D.; Wang, W.; Liu, J.; Holub, K. W.; Yang, R. Ultrafast Thermoreflectance Techniques for Measuring Thermal Conductivity and Interface Thermal Conductance of Thin Films. *J. Appl. Phys.* **2010,** *108* (9), 094315.

(64) Schmidt, A. J.; Chen, X.; Chen, G. Pulse Accumulation, Radial Heat Conduction, and Anisotropic Thermal Conductivity in Pump-Probe Transient Thermoreflectance. *Rev. Sci. Instrum.* **2008,** *79* (11), 114902.

(65) Liu, J.; Zhu, J.; Tian, M.; Gu, X.; Schmidt, A.; Yang, R. Simultaneous Measurement of Thermal Conductivity and Heat Capacity of Bulk and Thin Film Materials Using Frequency-Dependent Transient Thermoreflectance Method. *Rev. Sci. Instrum.* **2013,** *84* (3), 034902.

(66) Cahill, D. G. Analysis of Heat Flow in Layered Structures for Time-Domain Thermoreflectance. *Rev. Sci. Instrum.* **2004,** *75* (12), 5119-5122.

(67) Walter, J.; Wang, H.; Luo, B.; Frisbie, C.; Leighton, C. Electrostatic versus Electrochemical Doping and Control of Ferromagnetism in Ion-Gel-Gated Ultrathin $La_{0.5}Sr_{0.5}CoO_{3-\delta}$. *ACS Nano* **2016,** *10* (8), 7799.

(68) Aarbogh, H.; Wu, J.; Wang, L.; Zheng, H.; Mitchell, J.; Leighton, C. Magnetic and Electronic Properties of $La_{1-x}Sr_xCoO_3$ Single Crystals across the Percolation Metal-Insulator Transition. *Phys. Rev. B* **2006,** *74* (13), 134408.

(69) Wu, J.; Lynn, J.; Glinka, C.; Burley, J.; Zheng, H.; Mitchell, J.; Leighton, C. Intergranular Giant Magnetoresistance in a Spontaneously Phase Separated Perovskite Oxide. *Phys. Rev. Lett.* **2005,** *94* (3), 037201.

(70) He, C.; Eisenberg, S.; Jan, C.; Zheng, H.; Mitchell, J.; Leighton, C. Heat Capacity Study of Magnetoelectronic Phase Separation in $La_{1-x}Sr_xCoO_3$ Single Crystals. *Phys. Rev. B* **2009,** *80* (21), 214411.

(71) Wang, X.; Ho, V.; Segalman, R. A.; Cahill, D. G. Thermal Conductivity of High-Modulus Polymer Fibers. *Macromolecules* **2013,** *46* (12), 4937-4943.

(72) Wang, X.; Mori, T.; Kuzmych-Ianchuk, I.; Michiue, Y.; Yubuta, K.; Shishido, T.; Grin, Y.; Okada, S.; Cahill, D. G. Thermal Conductivity of Layered Borides: The Effect of Building Defects on the Thermal Conductivity of $TmAlB_4$ and the Anisotropic Thermal Conductivity of AlB_2. *APL Mater.* **2014,** *2* (4), 046113.

(73) Mai, C.-K.; Schlitz, R. A.; Su, G. M.; Spitzer, D.; Wang, X.; Fronk, S. L.; Cahill, D. G.; Chabinyc, M. L.; Bazan, G. C. Side-Chain Effects on the Conductivity, Morphology, and Thermoelectric Properties of Self-Doped Narrow-Band-Gap Conjugated Polyelectrolytes. *J. Am. Chem. Soc.* **2014,** *136* (39), 13478-13481.

(74) Liu, J.; Wang, X.; Li, D.; Coates, N. E.; Segalman, R. A.; Cahill, D. G. Thermal Conductivity and Elastic Constants of PEDOT: PSS with High Electrical Conductivity. *Macromolecules* **2015,** *48* (3), 585-591.

(75) Wang, X.; Liman, C. D.; Treat, N. D.; Chabinyc, M. L.; Cahill, D. G. Ultralow Thermal Conductivity of Fullerene Derivatives. *Phys. Rev. B* **2013,** *88* (7), 075310.

(76) Zhu, J.; Zhu, Y.; Wu, X.; Song, H.; Zhang, Y.; Wang, X. Structure-Thermal Property Correlation of Aligned Silicon Dioxide Nanorod Arrays. *Appl. Phys. Lett.* **2016,** *108* (23), 231903.

(77) Franz, R.; Wiedemann, G. Ueber die Wärme - Leitungsfähigkeit der Metalle. *Ann. Phys.* **1853,** *165* (8), 497-531.

(78) Kitel, C. Introduction to Solid State Physics. John Wiley & Sons, Inc: New York, U.S.A., 1971.

(79) Losego, M. D.; Moh, L.; Arpin, K. A.; Cahill, D. G.; Braun, P. V. Interfacial Thermal Conductance in Spun-Cast Polymer Films and Polymer Brushes. *Appl. Phys. Lett.* **2010,** *97* (1), 011908.

(80) Wu, X.; Ni, Y.; Zhu, J.; Burrows, N. D.; Murphy, C. J.; Dumitrica, T.; Wang, X. Thermal Transport across Surfactant Layers on Gold Nanorods in Aqueous Solution. *ACS Appl. Mater. Interfaces* **2016,** *8* (16), 10581-10589.

(81) Feng, T.; Ruan, X. Prediction of Spectral Phonon Mean Free Path and Thermal Conductivity with Applications to Thermoelectrics and Thermal Management: A Review. *J. Nanomater.* **2014,** *2014*.

(82) Read, M. S.; Islam, M. S.; Watson, G. W.; King, F.; Hancock, F. E. Defect Chemistry and Surface Properties of $LaCoO_3$. *J. Mater. Chem.* **2000,** *10* (10), 2298-2305.

(83) Cherry, M.; Islam, M. S.; Catlow, C. Oxygen Ion Migration in Perovskite-Type Oxides. *J. Solid State Chem.* **1995,** *118* (1), 125-132.

(84) Khan, S.; Oldman, R.; Cora, F.; Catlow, C.; French, S.; Axon, S. A Computational Modelling Study of Oxygen Vacancies at $LaCoO_3$ Perovskite Surfaces. *Phys. Chem. Chem. Phys.* **2006,** *8* (44), 5207-5222.

(85) Ziman, J. M. Electrons and Phonons: the Theory of Transport Phenomena in Solids; Oxford University Press, Oxford, England, U.K., 1960.

(86) Plimpton, S. Fast Parallel Algorithms for Short-Range Molecular Dynamics. *J. Comput. Phys.* **1995,** *117* (1), 1-19.

(87) Hohensee, G. T.; Hsieh, W.-P.; Losego, M. D.; Cahill, D. G. Interpreting Picosecond Acoustics in the Case of Low Interface Stiffness. *Rev. Sci. Instrum.* **2012,** *83* (11), 114902.

(88) Shi, J.; Dong, Y.; Fisher, T.; Ruan, X. Thermal Transport across Carbon Nanotube-Graphene Covalent and van der Waals Junctions. *J. Appl. Phys.* **2015,** *118* (4), 044302.

(89) Ratsifaritana, C.; Klemens, P. Scattering of Phonons by Vacancies. *Int. J. Thermophys.* **1987,** *8* (6), 737-750.

(90) Zhu, J.; Park, H.; Chen, J. Y.; Gu, X.; Zhang, H.; Karthikeyan, S.; Wendel, N.; Campbell, S. A.; Dawber, M.; Du, X.; Li, M.; Wang, J.-P.; Yang, R. G.; Wang, X. J. Revealing the Origins of 3D Anisotropic Thermal Conductivities of Black Phosphorus. *Adv. Electron. Mater.* **2016,** *2* (5), 1600040.

Supporting Information for

Glass-like Thermal Conductivity Induced by Oxygen Vacancies in Nanoscale Epitaxial $La_{0.5}Sr_{0.5}CoO_{3-\delta}$

X.W. Wu,[a] J. Walter,[b] T.L. Feng,[c] J. Zhu,[a] H. Zheng,[d] J.F. Mitchell,[d] N. Biškup,[e] M. Varela,[e] X.L. Ruan,[c] C. Leighton,[b] X.J. Wang,[*,a]

[a]Department of Mechanical Engineering, University of Minnesota, Twin Cities, 111 Church Street S.E., Minneapolis, MN 55455, USA

[b]Department of Chemical Engineering and Material Science, University of Minnesota, Twin Cities, 421 Washington Ave. S.E., Minneapolis, MN 55455, USA

[c]School of Mechanical Engineering and the Birck Nanotechnology Center, Purdue University, West Lafayette, IN 47907, USA

[d]Materials Science Division, Argonne National Laboratory, Argonne, IL 60439, USA

[e]Departamento de Fisica de Materiales & Instituto Pluridisciplinar, Universidad Complutense de Madrid, Madrid, 28040 Spain (Previous address: Materials Science & Technology division, Oak Ridge National Laboratory. Oak Ridge, TN 37831, USA)

[*]Corresponding Author:

Xiaojia Wang Email: wang4940@umn.edu

S1. Thermal Characterization with TDTR

The time-domain thermoreflectance data are collected with an ultrafast pump-probe laser system as shown in Figure S1. The optical excitation source is a mode-locked Ti: sapphire laser that produces a train of pulses (~100 fs) at a repetition rate of 80 MHz. All the samples are coated with thin films of Al to serve as metal transducers, which has a large thermoreflectance coefficient at the laser operating wavelength (780 nm) and provides good adhesion to the sample beneath. The laser beam is divided into a pump beam and a probe beam through a polarizing beamsplitter (PBS). A mechanical delay stage varies the optical path of the pump beam, producing a time delay of up to 4 ns between the pump excitation and probe sensing. A 5× objective lens is used to focus both the pump and probe beams on the sample surface with a beam spot size (radius) of $w_0 = 12\ \mu$m. Upon pump heating, the reflected probe beam from the sample is collected by a fast-response photodiode for further signal processing with an rf lock-in amplifier and LabVIEW program.

For data analysis, the thickness (h_{Al}), volumetric heat capacity (C_{Al}), and thermal conductivity (Λ_{Al}) of the Al transducer are input parameters. The thickness of the Al transducer is determined from picosecond acoustics (as illustrated in Fig. 2a),[1] and the values of C_{Al} are taken from the literature.[2] The thermal conductivity of the Al transducer is derived from the electrical conductivity measured by a four-point probe method, combined with the Wiedemann-Franz law, prior to the TDTR measurement. The thermal conductivities of all the samples are extracted by fitting the TDTR signals to a thermal diffusion model.[3]

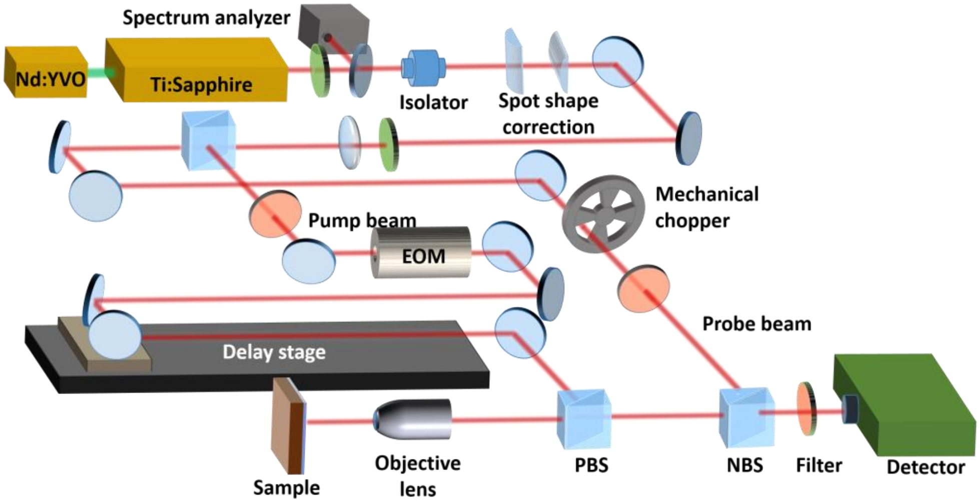

Figure S1. Schematic diagram of the TDTR experimental setup.

S2. Boltzmann's Transport Equation Model

The phonon frequency and group velocity are calculated using a Lattice Dynamics (LD) program with a hybrid interatomic potential that is described by the core-shell model, short-range Buckingham potential, and long-range Coulombic forces.[4] This hybrid potential has demonstrated excellent reproducibility of the lattice structure, mechanistic features, vacancy energy, doping energy, oxygen ion migration energy, and surface polarization.[4-6] The lattice constants of $LaCoO_3$ (LCO) relaxed from our potential are a = b = 5.410 Å, c = 13.239 Å, which agree reasonably well with the experimental results a = b = 5.426, c = 12.991 Å.[7-8] The phonon dispersion of LCO obtained by this potential, calculated by using the General Utility Lattice Program (GULP),[9] is shown in Figure S2. $LaCoO_3$ is a *R-3c* phase crystal with rhombohedral (Rh.) structure, and it has 10 basis atoms and 30 phonon branches. While $La_{0.5}Sr_{0.5}CoO_3$ may technically be a *R*-3*c* phase crystal it is very close to cubic (i.e. $\alpha_R \approx 60°$), and it has 20 basis atoms and 60 phonon branches. The dispersion is found to agree well with both first-principles calculations[10] and experimental inelastic neutron scattering data.[11]

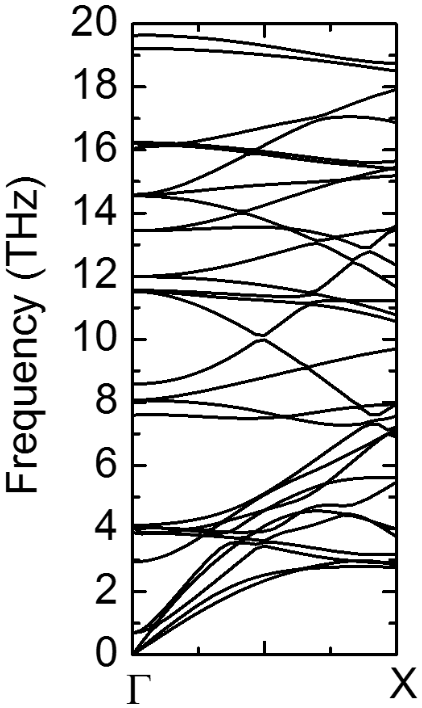

Figure S2. The phonon dispersions of LCO calculated from lattice dynamics using the hybrid potential.

Each of the terms in the phonon relaxation time τ (Eq. 2) are calculated as follows:

$$\frac{1}{\tau_{\mathrm{p}}(\mathbf{k},\nu)}=\frac{A\gamma^2 k_{\mathrm{B}}T}{M_{\mathrm{a}}v^2(\mathbf{k},\nu)}\frac{\omega^2(\mathbf{k},\nu)}{\omega_{\max}(\nu)}\exp\left(-\frac{\hbar\omega_{\max}(\nu)}{3k_{\mathrm{B}}T}\right) \tag{S1}$$

$$\frac{1}{\tau_{\mathrm{Sr}}(\mathbf{k},\nu)}=\frac{\pi}{2}g_{\mathrm{Sr}}\omega^2(\mathbf{k},\nu)\,\mathrm{DOS}(\omega) \tag{S2}$$

$$\frac{1}{\tau_{\mathrm{O_V}}(\mathbf{k},\nu)}=\frac{\pi}{2}g_{\mathrm{O_V}}\omega^2(\mathbf{k},\nu)\,\mathrm{DOS}(\omega) \tag{S3}$$

$$\frac{1}{\tau_{\mathrm{b}}(\mathbf{k},\nu)}=\frac{1-p}{1+p}\frac{v(\mathbf{k},\nu)}{h} \tag{S4}$$

For the phonon-phonon scattering[12] in Eq. (S1), $\omega_{\max}(\nu)$ is the maximum frequency of the phonon branch ν. γ is the Grüneisen parameter. M_{a} is the average atomic mass, given by

$$M_{\mathrm{a}} = \frac{\alpha_{\mathrm{La}} M_{\mathrm{La}} + \alpha_{\mathrm{Sr}} M_{\mathrm{Sr}} + \alpha_{\mathrm{Co}} M_{\mathrm{Co}} + \alpha_{\mathrm{O}} M_{\mathrm{O}}}{\alpha_{\mathrm{La}} + \alpha_{\mathrm{Sr}} + \alpha_{\mathrm{Co}} + \alpha_{\mathrm{O}}} \tag{S5}$$

where α is the stoichiometric coefficient. $A\gamma^2$ is a fitting parameter which can be obtained by fitting the thermal conductivity of pure LCO to 15 W m^{-1} K^{-1}, and ~16 W m^{-1} K^{-1} for STO and LAO at room temperature. The best fit of $A\gamma^2$ is 8.3.

For the mass disorder due to impurity or defect scattering[13] in Eqs. (S2)-(S3), the DOS(ω) is the normalized phonon density of states which is shown in Figure S3. It is noticeable that the Debye model DOS(ω) $\propto$ ω^2 is only valid for the low energy phonons (up to 3 THz). Thus, compared to the Callaway model which assumes the Debye dispersion, Eqs. (S2) - (S3) are more accurate in capturing the alloy and impurity scattering for many systems.[14-18] g_{sr} represents the alloying mass disorder induced by the mass difference between La and Sr atoms, given by

$$g_{\mathrm{Sr}} = \frac{\alpha_{\mathrm{Sr}}}{\alpha_{\mathrm{La}} + \alpha_{\mathrm{Sr}}}\left(1 - \frac{M_{\mathrm{Sr}}}{\bar{M}_{\mathrm{LaSr}}}\right)^2 + \frac{\alpha_{\mathrm{La}}}{\alpha_{\mathrm{La}} + \alpha_{\mathrm{Sr}}}\left(1 - \frac{M_{\mathrm{La}}}{\bar{M}_{\mathrm{LaSr}}}\right)^2 \tag{S6}$$

$$\bar{M}_{\mathrm{LaSr}} = \frac{\alpha_{\mathrm{La}} M_{\mathrm{La}} + \alpha_{\mathrm{Sr}} M_{\mathrm{Sr}}}{\alpha_{\mathrm{La}} + \alpha_{\mathrm{Sr}}} \tag{S7}$$

where g_{Ov} represents the oxygen vacancy effect, given by

$$g_{\mathrm{O_V}} = \frac{\delta}{3}\left(\frac{M_{\mathrm{O}}}{\bar{M}_{\mathrm{O}}}\right)^2 \cdot 3 \tag{S8}$$

$$\bar{M}_{\mathrm{O}} = \frac{3-\delta}{3} M_{\mathrm{O}} \tag{S9}$$

The factor 3 in Eq. (S8) accounts for the potential energy change due to the missing bond.[19] Thus $g_{\mathrm{Ov}} = 0.107$ for $\delta = 0.1$, and $g_{\mathrm{sr}} = 0.036$ for $x = 0.3$.

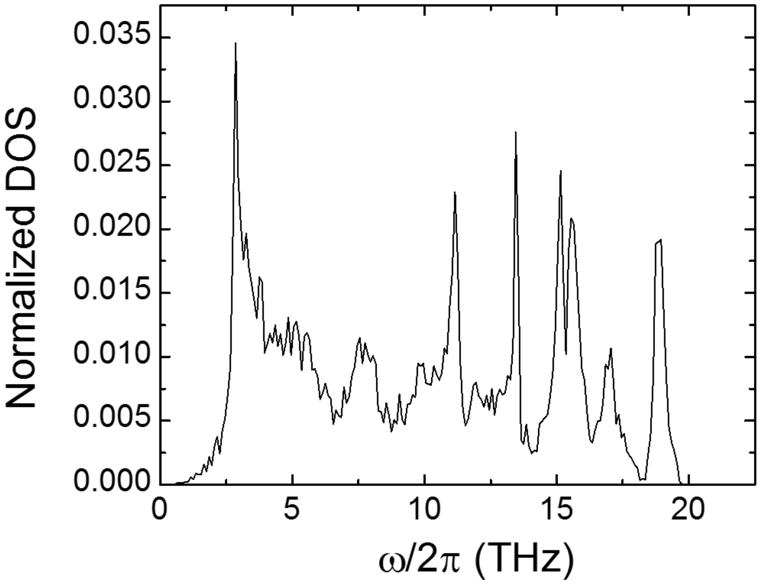

Figure S3. Normalized phonon DOS of LCO calculated from LD using the hybrid potential.

The film boundary scattering[15] in Eq. (S4) is determined by the film thickness *h* and the specularity parameter *p*, with $p = 0$ representing a diffuse surface and $p = 1$ representing a mirror-like surface. For through-plane transport, *p* is taken as 0.

Figure S4 illustrates the phonon relaxation time spectra for LCO and $La_{0.5}Sr_{0.5}CoO_{2.9}$ (LSCO) calculated from the BTE model. We find that the Sr alloying and oxygen vacancies mainly block the high-energy phonons (>3 THz), of which the relaxation time reduces from a few picoseconds to shorter than 1 ps, while the low-energy phonons are less influenced. We see that most of the phonons have a relaxation time shorter than 8 ps for both LCO and LSCO. This BTE result supports our MD simulation setup in which the autocorrelation length is set as 100 ps, much longer than phonon relaxation time. Also, we can see that the heat current auto-correlation functions (HCACFs) shown in Fig. S5 converge after a few picoseconds, which is consistent with our BTE results.

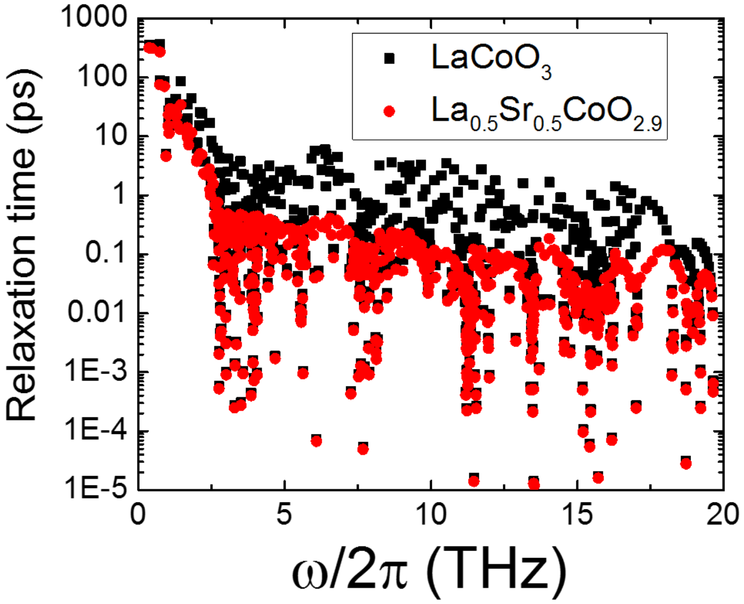

Figure S4. The phonon relaxation time spectra for LCO and $La_{0.5}Sr_{0.5}CoO_{2.9}$ calculated from the BTE model.

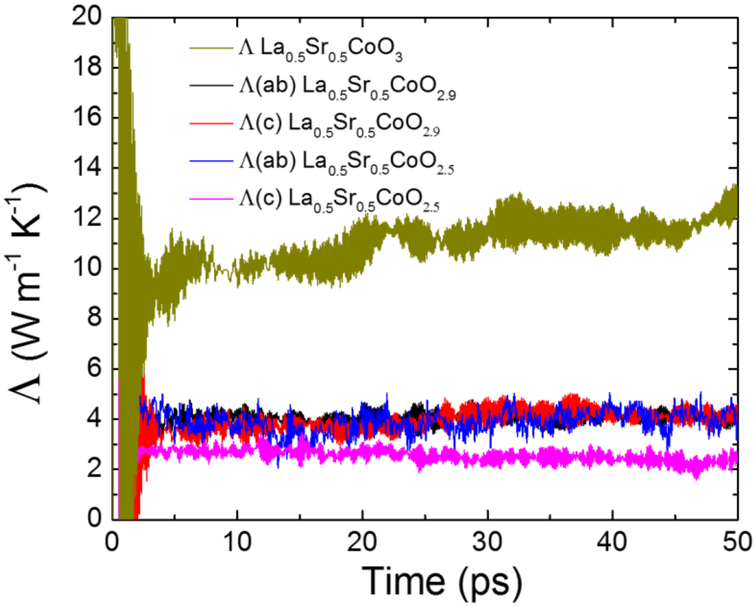

Figure S5. The HCACFs of LSCO samples calculated from GKMD simulations

S3. Molecular Dynamics Simulations

In the MD simulation, the time step interval is set as 0.5 fs (2,000 THz) which is short enough to resolve all the phonon frequencies. In each simulation, the system is first run in a constant pressure and temperature ensemble (NPT) for 400,000 steps to reach thermal equilibrium, and then it switches to the constant volume and energy ensemble (NVE) and runs for 400,000 steps again to stabilize the system. Next, 4,000,000 steps of NVE computation, covering 2 ns, are used to calculate the heat current and thermal conductivity. The autocorrelation duration is set as 100 ps, which is long enough to obtain converged HCACF since most phonon relaxation times are far below 100 ps. The simulation domain is a cubic box consisting of 12×12×12 cells with 8640 atoms (if no vacancies), which is large enough to get a converged thermal conductivity since Equilibrium MD with periodic boundary conditions is less affected by domain size than Non-equilibrium MD.

The phonon dispersion is calculated using LD without the core-shell model and the results are compared with experimental values in Figure S6.

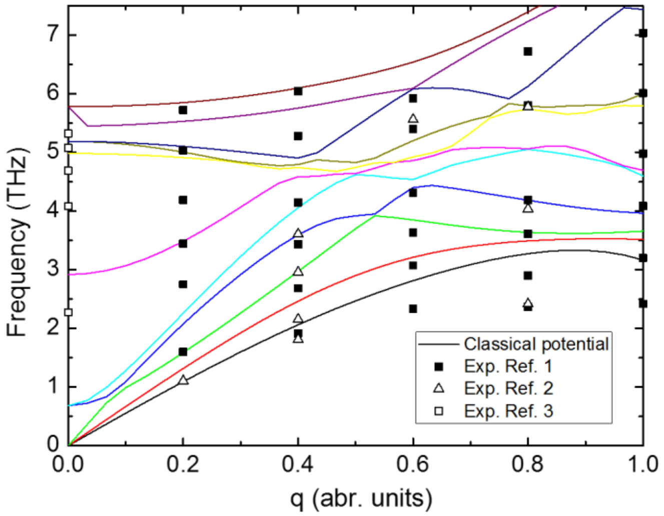

Figure S6. The phonon dispersion for LCO calculated from LD using the potential without core-shell model. The dots are the experimental data taken from Ref. [11] (solid square), Ref. [20] (open triangle), and Ref. [21] (open square).

According to Ref. [4], the charge (nominal valence) of some Co ions changes from +3 to +4 after doping with Sr, and from +3 to +2 after removing O ions. Therefore, in the MD simulations, we increase the charges of the 8 Co atoms surrounding the Sr atom by +1, and reduce the charges of the 2 Co atoms near oxygen vacancies by +1.

S4. Uncertainty of Λ_{eff} and Λ_{LSCO} Obtained from the Experiment

In the experimental method, we utilize a straight-line model to extract the intrinsic thermal conductivity of LSCO. The straight-line model converted from Eq. (1) is

$$y(x) = a + bx \tag{S10}$$

where $x = h_{\text{LSCO}}$, $y(x) = R_{\text{eff}} = h_{\text{LSCO}} / \Lambda_{\text{eff}}$. $a = 1/\Lambda_{\text{LSCO}}$ and $b = R_{\text{I1}} + R_{\text{I2}}$ are the slope and y-axis intercept of the straight line respectively. These are assumed to be constants according to the approximation of a thickness-independent interfacial thermal resistance and of an intrinsic LSCO thermal conductivity, as described in the section 3.1 of the manuscript.

Λ_{eff} is obtained directly from TDTR measurement. To evaluate the uncertainty of Λ_{eff}, we calculate the sensitivity of the TDTR measurements to various parameters in the thermal model used for the TDTR analysis.^{22} The sensitivity parameters S_α is defined as

$$S_\alpha = \frac{\partial \text{In}(R)}{\partial \text{In}(\alpha)} \tag{S11}$$

where R is the magnitude of the ratio of in-phase and out-of-phase signals from the lock-in amplifier ($-V_{\text{in}}/V_{\text{out}}$) and α is the parameter in the thermal model.^{22} The uncertainty of the effective thermal conductivity Λ_{eff} measured by TDTR can be estimated by taking into account individual uncertainties based on the error propagation formula,

$$\left(\frac{\Delta\Lambda_{\text{eff}}}{\Lambda_{\text{eff}}}\right)^2 = \sum\left(\frac{S_\alpha}{S_{\Lambda_{\text{eff}}}}\frac{\Delta\alpha}{\alpha}\right)^2 \qquad \text{(S12)}$$

where $\Delta\Lambda_{\text{eff}} / \Lambda_{\text{eff}}$ is the uncertainty of Λ_{eff}, and $\Delta\alpha / \alpha$ is the uncertainty of parameter α. The calculated uncertainties of Λ_{eff} range from 11% to 15% for samples of LSCO epitaxial films with different thicknesses, on LAO or STO substrates.

In the straight-line model fitting of Eq. (S10), the uncertainty of $y(x) = R_{\text{eff}} = h_{\text{LSCO}} / \Lambda_{\text{eff}}$ at each data point can be obtained by

$$\frac{\Delta R_{\text{eff}}}{R_{\text{eff}}} = \sqrt{\left(\frac{\Delta h_{\text{LSCO}}}{h_{\text{LSCO}}}\right)^2 + \left(\frac{\Delta\Lambda_{\text{eff}}}{\Lambda_{\text{eff}}}\right)^2} \qquad \text{(S13)}$$

where $\Delta h_{\text{LSCO}} / h_{\text{LSCO}}$ is the uncertainty of thickness of the LSCO epitaxial films.

The Λ_{LSCO} is extracted through linear regression by Eq. (S10), and its uncertainty should take into account the standard deviation of the data points to the fitted straight line, as well as the uncertainty associated with each measurement $y_i = R_{\text{eff}}$ obtained from Eq. (S13). To measure how well the model agrees with the data, we use the chi-square merit function χ^2 defined as [23]

$$\chi^2(a,b) = \sum_{i=1}^{N}\left(\frac{y_i - b - ax_i}{\sigma_i}\right)^2 \qquad \text{(S14)}$$

where σ_i is the absolute uncertainty of y_i, and N is number of total points used for the straight-line fitting, which is four in our experiment method.

The values of a and b can be determined when Eq. (S14) is minimized. Under this condition, derivatives of $\chi^2(a,b)$ with respect to a and b should vanish.[23]

$$0 = \frac{\partial\chi^2}{\partial a} = -2\sum_{i=1}^{N}\frac{x_i(y_i - b - ax_i)}{\sigma_i^2} \qquad \text{(S15)}$$

$$0 = \frac{\partial \chi^2}{\partial b} = -2\sum_{i=1}^{N} \frac{y_i - b - ax_i}{\sigma_i^2} \tag{S16}$$

For convenience, the following sums are defined:

$$\begin{aligned} &S \equiv \sum_{i=1}^{N} \frac{1}{\sigma_i^2} \quad S_x \equiv \sum_{i=1}^{N} \frac{x_i}{\sigma_i^2} \quad S_y \equiv \sum_{i=1}^{N} \frac{y_i}{\sigma_i^2} \\ &S_{xx} \equiv \sum_{i=1}^{N} \frac{x_i^2}{\sigma_i^2} \quad S_{xy} \equiv \sum_{i=1}^{N} \frac{x_i y_i}{\sigma_i^2} \end{aligned} \tag{S17}$$

Then the solutions of Eqs. (S15) and (S16) can be obtained as

$$\Delta \equiv SS_{xx} - (S_x)^2 \tag{S18}$$

$$a = \frac{SS_{xy} - S_x S_y}{\Delta} \tag{S19}$$

$$b = \frac{S_{xx} S_y - S_x S_{xy}}{\Delta} \tag{S20}$$

Eqs. (S19) and (S20) give the solutions for the best-fit model parameters *a* and *b*. With the expressions of *a* and *b*, we can determine their uncertainties through the error propagation. For a series of independent data points, each data point contributes its individual uncertainty to the parameters.[23] For function $f = (y_1, y_2, \ldots y_i, \ldots y_N)$, the variance σ_f^2 can be calculated as

$$\sigma_f^2 = \sum_{i=1}^{N} \sigma_i^2 \left(\frac{\partial f}{\partial y_i}\right)^2 \tag{S21}$$

For a straight line, we take the derivatives of *a* and *b* with respect to y_i through Eqs. (S19) and (S20) and then sum over all points as in Eq. (S21)

$$\sigma_a = \sqrt{S / \Delta} \tag{S22}$$

$$\sigma_b = \sqrt{S_{xx} / \Delta} \tag{S23}$$

which are the uncertainties in the estimates of *a* and *b*, respectively.

With the obtained uncertainties of a and b, we can calculate the relative uncertainty of Λ_{LSCO} through

$$\frac{\Delta\Lambda_{\mathrm{LSCO}}}{\Lambda_{\mathrm{LSCO}}} = \sqrt{(\frac{\Delta a}{a})^2} \qquad \text{(S24)}$$

The calculated relative uncertainties of Λ_{LSCO} are 37% for the LSCO/LAO epitaxial thin films (sample A in Table I) and 40% for the LSCO/STO epitaxial thin films (sample B in Table I). The relative uncertainties of $R_{\mathrm{I1}}+R_{\mathrm{I2}}$ are 27% and 24% for samples A and B, respectively.

We notice that the relative uncertainties for Λ_{LSCO} and $R_{\mathrm{I1}} + R_{\mathrm{I2}}$ are overestimated when derived using the individual uncertainty of each data point. In previous experimental publications using straight line fitting to extract the thin-film's intrinsic thermal conductivity,[24] we seldom found any discussion on the uncertainty analysis of fitted parameters taking into account the uncertainty of each data point. So here we provide a conservatively large estimation for the uncertainty in the intrinsic thermal conductivity and combined interfacial thermal resistances. For reference, we also provide the relative uncertainties for Λ_{LSCO} ($\Delta\Lambda_{\mathrm{LSCO}}/\Lambda_{\mathrm{LSCO}}$) and $R_{\mathrm{I1}}+R_{\mathrm{I2}}$ [$\Delta(R_{\mathrm{I1}}+R_{\mathrm{I2}})/(R_{\mathrm{I1}}+R_{\mathrm{I2}})$] derived from the standard deviation of the data points without taking into account of the uncertainty of each data point. In this case, the values of $\Delta\Lambda_{\mathrm{LSCO}} / \Lambda_{\mathrm{LSCO}}$ are 15% for sample A and 13% for the sample B. The relative uncertainties of $R_{\mathrm{I1}}+R_{\mathrm{I2}}$ are 12% and 9% for samples A and B, respectively.

S5. Depth dependence of δ and x_{eff}

The depth dependence of δ and the effective doping value, x_{eff}, were estimated by analyzing previously published electron energy loss spectroscopy (EELS) data[25] for Type B samples and new EELS data on Type A samples. For Type B samples, this involved taking the depth dependence of the O 2p hole peak intensity ($I_{\text{h-peak}}$, determined from the pre-peak on the O K edge) from Fig. 3e of Ref. [25] and converting it to an x_{eff} using the calibration from bulk LSCO single crystals shown in the inset of Fig. 3b of Ref. [25] ($I_{\text{h-peak}} = 0.45x_{\text{eff}}$). With x_{eff} determined, we used $x_{\text{eff}} = x - 2\delta$ (*i.e.*, compensation of Sr-induced holes by O vacancies) to calculate δ, assuming the Sr level to be $x = 0.5$ and depth independent, as justified by Fig. 3g of Ref. [25]. The same procedure was followed using new EELS data for Type A samples. Fig. S7 below shows the results for 35-45 nm thick films on LAO and STO substrates. In the 3-18 nm range relevant to the thinner films studied in this paper we find $\delta \approx 0.09$ on LAO (type A samples) and δ averaging to approximately 0.11 on STO (type B samples). These are the values quoted in the main paper.

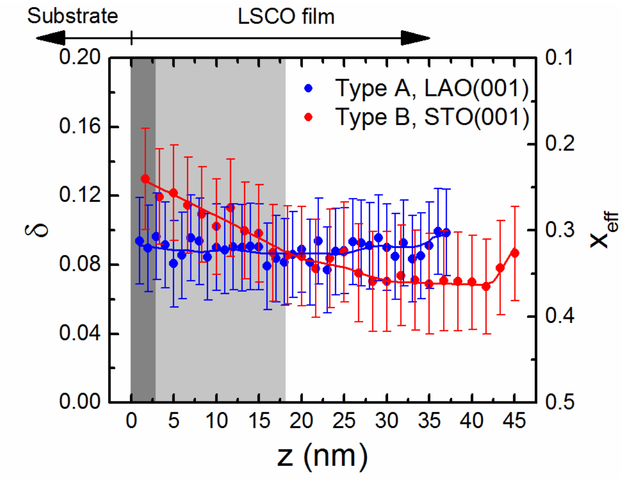

Figure S7. The depth dependence of the oxygen vacancy density (δ) and the effective doping level ($x_{\text{eff}} = x - 2\delta$). Blue and red symbols represent Type A and Type B samples respectively. The solid blue and red lines are guides to the eye. The light gray region represents the thickness range probed with time-domain thermoreflectance and the dark gray portion represents the interface region described in the main text.

References

(1) Eesley, G. L.; Clemens, B. M.; Paddock, C. A. Generation and Detection of Picosecond Acoustic Pulses in Thin Metal Films. *Appl. Phys. Lett.* **1987,** *50* (12), 717-719.

(2) Ditmars, D.; Plint, C.; Shukla, R. Aluminum. I. Measurement of the Relative Enthalpy from 273 to 929 K and Derivation of Thermodynamic Functions for Al(s) from 0 K to Its Melting Point. *Int. J. Thermophys.* **1985,** *6* (5), 499-515.

(3) Cahill, D. G. Analysis of Heat Flow in Layered Structures for Time-Domain Thermoreflectance. *Rev. Sci. Instrum.* **2004,** *75* (12), 5119-5122.

(4) Read, M. S.; Islam, M. S.; Watson, G. W.; King, F.; Hancock, F. E. Defect Chemistry and Surface Properties of $LaCoO_3$. *J. Mater. Chem.* **2000,** *10* (10), 2298-2305.

(5) Cherry, M.; Islam, M. S.; Catlow, C. Oxygen Ion Migration in Perovskite-Type Oxides. *J. Solid State Chem.* **1995,** *118* (1), 125-132.

(6) Khan, S.; Oldman, R.; Cora, F.; Catlow, C.; French, S.; Axon, S. A Computational Modelling Study of Oxygen Vacancies at $LaCoO_3$ Perovskite Surfaces. *Phys. Chem. Chem. Phys.* **2006,** *8* (44), 5207-5222.

(7) Radaelli, P. G.; Cheong, S.-W. Structural Phenomena Associated with the Spin-State Transition in $LaCoO_3$. *Phys. Rev. B* **2002,** *66* (9), 094408.

(8) Chainani, A.; Mathew, M.; Sarma, D. Electron-Spectroscopy Study of the Semiconductor-Metal Transition in $La_{1-x}Sr_xCoO_3$. *Phys. Rev. B* **1992,** *46* (16), 9976.

(9) Gale, J. D.; Rohl, A. L. The General Utility Lattice Program (GULP). *Mol. Simulat.* **2003,** *29* (5), 291-341.

(10) Laref, A.; Luo, J. S. Magnetic Excitation and Phonon Dispersion in $LaCoO_3$ Compound. *J. Phys. Soc. JPN.* **2010,** *79* (6), 064702.

(11) Rybina, A.; Efimov, V.; Alekseev, P.; Troyanchuk, I.; Ivanov, A.; Sikolenko, V.; Clementyev, E. Inelastic Neutron Scattering Study of the Lattice Dynamics of $LaCoO_3$. *J. Surf. Investig-X-RA.* **2011,** *5* (6), 1140-1143.

(12) Slack, G. A.; Galginaitis, S. Thermal Conductivity and Phonon Scattering by Magnetic Impurities in CdTe. *Phys. Rev.* **1964,** *133* (1A), A253.

(13) Tamura, S.-i. Isotope Scattering of Dispersive Phonons in Ge. *Phys. Rev. B* **1983,** *27* (2), 858.

(14) Garg, J.; Bonini, N.; Kozinsky, B.; Marzari, N. Role of Disorder and Anharmonicity in the Thermal Conductivity of Silicon-Germanium Alloys: A First-Principles Study. *Phys. Rev. Lett.* **2011,** *106* (4), 045901.

(15) Feng, T.; Ruan, X. Prediction of Spectral Phonon Mean Free Path and Thermal Conductivity with Applications to Thermoelectrics and Thermal Management: A Review. *J. Nanomater.* **2014,** *2014*.

(16) Kamitakahara, W.; Brockhouse, B. Vibrations of a Mixed Crystal: Neutron Scattering from $Ni_{55}Pd_{45}$. *Phys. Rev. B* **1974,** *10* (4), 1200.

(17) Lindsay, L.; Broido, D.; Reinecke, T. Thermal Conductivity and Large Isotope Effect in GaN from First Principles. *Phys. Rev. Lett.* **2012,** *109* (9), 095901.

(18) Feng, T.; Qiu, B.; Ruan, X. Coupling between Phonon-Phonon and Phonon-Impurity Scattering: A Critical Revisit of the Spectral Matthiessen's Rule. *Phys. Rev. B* **2015,** *92* (23), 235206.

(19) Ratsifaritana, C.; Klemens, P. Scattering of Phonons by Vacancies. *Int. J. Thermophys.* **1987,** *8* (6), 737-750.

(20) Kobayashi, Y.; Naing, T. S.; Suzuki, M.; Akimitsu, M.; Asai, K.; Yamada, K.; Akimitsu, J.; Manuel, P.; Tranquada, J.; Shirane, G. Inelastic Neutron Scattering Study of Phonons and Magnetic Excitations in $LaCoO_3$. *Phys. Rev. B* **2005,** *72* (17), 174405.

(21) Ishikawa, A.; Nohara, J.; Sugai, S. Raman Study of the Orbital-Phonon Coupling in $LaCoO_3$. *Phys. Rev. Lett.* **2004,** *93* (13), 136401.

(22) Koh, Y. K. Doctoral Disseration, Heat Transport by Phonons in Crystalline Materials and Nanostructures. University of Illinois at Urbana-Champaign, U.S.A., 2011.

(23) Press, W. H.; Teukolsky, S. A.; Vetterling, W. T.; Flannery, B. P. Numerical recipes in C; 2nd Ed.; Cambridge University Press, Cambridge, U.K., 1996; pp. 657-668.

(24) Losego, M. D.; Moh, L.; Arpin, K. A.; Cahill, D. G.; Braun, P. V. Interfacial Thermal Conductance in Spun-Cast Polymer Films and Polymer Brushes. *Appl. Phys. Lett.* **2010,** *97* (1), 011908.

(25) Torija, M. A.; Sharma, M.; Gazquez, J.; Varela, M.; He, C.; Schmitt, J.; Borchers, J. A.; Laver, M.; El-Khatib, S.; Leighton, C. Chemically Driven Nanoscopic Magnetic Phase Separation at the $SrTiO_3$(001)/$La_{1-x}Sr_xCoO_3$ Interface. *Adv. Mater.* **2011,** *23* (24), 2711-2715.